Astronomy & Astrophysics manuscript no. starsim_p1_v8
November 23, 2015
©ESO 2015

arXiv:1511.06717v1 [astro-ph.EP] 20 Nov 2015

Modelling the photosphere of active stars for planet detection and characterization

Enrique Herrero[1], Ignasi Ribas[1], Carme Jordi[2], Juan Carlos Morales[3], Manuel Perger[1], and Albert Rosich[1,2,4]

[1] Institut de Ciències de l'Espai (CSIC-IEEC), Campus UAB, Carrer de Can Magrans s/n, 08193 Cerdanyola del Vallès, Spain, e-mail: eherrero@ice.cat, iribas@ice.cat, perger@ice.cat, rosich@ice.cat
[2] Dept. d'Astronomia i Meteorologia, Institut de Ciències del Cosmos (ICC), Universitat de Barcelona (IEEC-UB), Martí Franquès 1, E08028 Barcelona, Spain, e-mail: carme.jordi@ub.edu
[3] LESIA-Observatoire de Paris, CNRS, UPMC Univ. Paris 06, Univ. Paris-Diderot, 5 Pl. Jules Janssen, 92195 Meudon CEDEX, France, e-mail: Juan-Carlos.Morales@obspm.fr
[4] Reial Acadèmia de Ciències i Arts de Barcelona (RACAB), Barcelona, Spain

Received <date> / Accepted <date>

ABSTRACT

Context. Stellar activity patterns are responsible for jitter effects that are observed at different timescales and amplitudes in the measurements obtained from photometric and spectroscopic time series observations. These effects are currently in the focus of many exoplanet search projects, since the lack of a well-defined characterization and correction strategy hampers the detection of the signals associated with small exoplanets.

Aims. Accurate simulations of the stellar photosphere based on the most recent available models for main sequence stars can provide synthetic photometric and spectroscopic time series data. These may help to investigate the relation between activity jitter and stellar parameters when considering different active region patterns. Moreover, jitters can be analysed at different wavelength scales (defined by the passbands of given instruments or space missions) in order to design strategies to remove or minimize them.

Methods. In this work we present the StarSim tool, which is based on a model for a spotted rotating photosphere built from the integration of the spectral contribution of a fine grid of surface elements. The model includes all significant effects affecting the flux intensities and the wavelength of spectral features produced by active regions and planets. The resulting synthetic time series data generated with this simulator are used in order to characterize the effects of activity jitter in extrasolar planet measurements from photometric and spectroscopic observations.

Results. Several cases of synthetic data series for Sun-like stars are presented to illustrate the capabilities of the methodology. A specific application for the characterization and modelling of the spectral signature of active regions is considered, showing that the chromatic effects of faculae are dominant for low temperature contrasts of spots. Synthetic multi-band photometry and radial velocity time series are modelled for HD 189733 by adopting the known system parameters and fitting for the map of active regions with StarSim. Our algorithm reproduces both the photometry and the RVs to good precision, generally better than the studies published to date. We evaluate the RV signature of the activity in HD 189733 by exploring a grid of solutions from the photometry. We find that the use of RV data in the inverse problem could break degeneracies and allow for a better determination of some stellar and activity parameters, e.g., the configuration of active regions, the temperature contrast of spots and the amount of faculae. In addition, the effects of spots are studied for a set of simulated transit photometry, showing that these can introduce variations in R_p/R_* measurements with a spectral signature and amplitude which are very similar to the signal of an atmosphere dominated by dust.

Key words. stars: activity – stars: rotation – stars: starspots

1. Introduction

Stellar activity in late-type main sequence stars induces photometric modulations and apparent radial velocity (thereafter RV) variations that may hamper the detection of Earth-like planets (Lagrange et al. 2010; Meunier et al. 2010a) and the measurement of their transit parameters (Barros et al. 2013), mass and atmospheric properties. A number of recent studies have been focused on trying to separate the small exoplanetary signals and the variations in the stellar signal both on light and RV curves (Dumusque 2014; Haywood et al. 2014; Robertson & Mahadevan 2014). However, we still lack detailed understanding of these stellar variations from the astrophysical point of view.

Late-type stars (i.e., late-F, G, K and M spectral types) are known to be variable to some extent due to the effects of activity. These effects are seen in the stellar photosphere in the form of spots and faculae, but we lack an accurate model of their signature on time series photometric and spectroscopic data. The signal of these activity patterns is modulated by the stellar rotation period. However, other phenomena also exist that may induce periodic signals in photometric and RV data. Pulsations, granulation, long term evolution of active regions and magnetic cycles may limit the capabilities of some planet searches. Such effects need to be subtracted or accounted for the design of survey strategies (Dumusque et al. 2011b,a; Moulds et al. 2013).

Significant improvement in our knowledge of activity effects on starlight will be crucial to make the most out of present and future planet search spectrographs (HARPS, HARPS-N, CARMENES, ESPRESSO, HIRES, APF, SPIRou) and transit observations from space (CHEOPS, PLATO, JWST). The most up-to-date and comprehensive information on stellar variability comes from studies of the Kepler mission, which are based on

the observation and analysis of ∼150,000 stars taken from the first Kepler data release. Ciardi et al. (2011) have found that 80% of M dwarfs have light dispersion less than 500 ppm over a period of 12 hours, while G dwarfs are the most stable group down to 40 ppm. McQuillan et al. (2012) investigates the variability properties of main sequence stars in the Kepler data, finding that the typical amplitude and time-scale increase towards later spectral types, which could be related to an increase in the characteristic size and life-time of active regions. Kepler operates in the visible (430 to 890 nm) where stellar photometric variability is at least a factor of 2 higher than in the near and thermal IR (the "sweet spot" for the characterization of exoplanet atmospheres) due to the increasing contrast between spots and the stellar photosphere with decreasing wavelength. Timescales for stellar activity are generally different from those associated with single transit observations (a few hours) and so removal of this spectral variability is possible. As a case in point, photometric modulations in the host of CoRoT-7 b are of the order of 2% (Lanza et al. 2010) and yet a transit with a depth of 0.03% was identified (Léger et al. 2009). Analysis of observations from Kepler have yielded comparable results.

The impact of stellar activity effects is very different in the case of primary (transit) and occultation observations. Alterations in the spot distribution across the stellar surface can modify the transit depth because of possible spot crossing events and also the changing ratio of photosphere and spotted areas on the face of the star (Oshagh et al. 2013b; Daassou et al. 2014). This can give rise to spurious planetary radius variations when multiple transit observations are considered. Correction of this effect requires the use of very quiet stars or precise modelling of the stellar surface using external constraints (McCullough et al. 2014; Oshagh et al. 2013a, 2014). The situation is much simpler for occultations, where the planetary emission follows directly from the transit depth measurement. In this case, only activity-induced variations on the timescale of the duration of the occultation need to be corrected to ensure that the proper stellar flux baseline is used. In the particular case of exoplanet characterization space missions, photometric monitoring in the visible will help in the correction of activity effects in the near and thermal IR, where the planet signal is higher.

The effects of stellar activity on time series data have also been the subject of several recent studies using different methods for modelling observations of spotted stars (Lanza et al. 2003, 2010; Desort et al. 2007; Aigrain et al. 2012; Meunier et al. 2010a; Kipping 2012). Examples are the SOAP (Boisse et al. 2012) and SOAP 2.0 (Dumusque et al. 2014) codes, which implement surface integration techniques to reproduce the cross-correlation function (CCF) of an active star by using a Gaussian function or real observed solar CCFs. These include the effects of Doppler shifts and convective blueshift inhibition produced by spots and faculae, as well as the limb brightening effect of faculae and a quadratic limb darkening law for the quiet photosphere. As discussed by Dumusque et al. (2014), it is essential to reproduce convective blueshift effects from real line shapes to obtain accurate RV variations. However, most of the codes only consider the effect caused by the flux differential of active regions (Boisse et al. 2012; Oshagh et al. 2013a, 2014). Desort et al. (2007) use Kurucz models together with a black-body approximation to reproduce the flux effect of spots on photometry and radial velocities, but they do not model the effects of convection inhibition in active regions. Moreover, most works reproduce the spectroscopic measurements from a single spectral line or generate the CCF from a simple gaussian model. These types of models do not preserve all the spectral information of spots and faculae, and therefore do not allow for the study of RV jitter produced at different spectral ranges, and the chromatic flux variations induced by activity.

In this work we present the `StarSim` tool, which investigates the effects of stellar activity on spectroscopic or spectrophotometric observations by simulating full spectra from the spotted photosphere of a rotating star. We use atmosphere models for low mass stars to generate synthetic spectra for the stellar surface, including the quiet photosphere, spots and faculae. The spectrum of the entire visible face of the star is obtained by summing the contribution of a grid of small surface elements and by considering their individual signals. Using such simulator, time series spectra can be obtained covering any time interval (e.g., the rotation period of the star or longer). By multiplying the spectra with the specific transfer function, both accounted for the atmospherical and the instrumental response, the methodology can be used to study the chromatic effects of spots and faculae on photometric modulations and spectroscopic jitters. The results are used to investigate methodologies to correct or mitigate the effects of activity on spectrophotometric time series data. Some of these methods are presented and discussed considering the case of HD 189733 in Sect.5. Our results will allow us to evaluate the effects of activity patterns on the stellar flux and hence define the best strategies to optimize exoplanet searches and measurement experiments.

This paper is the first of a series presenting several activity simulating and modelling applications of `StarSim` to improve our capabilities for planet detection and characterization.

2. Simulation of the photosphere of active stars

2.1. The models

2.1.1. Phoenix synthetic spectra

Among the most recent model atmosphere grids, we use spectra from the BT-Settl database (Allard et al. 2013) generated with the Phoenix code. These are used to reproduce the spectral signal for the different elements in the photosphere (quiet photosphere, spots and faculae) by considering different temperatures for the synthetic spectra. Models include revised solar oxygen abundances (Caffau et al. 2011) and a cloud formation recipe, which manage to reproduce the photometric and spectroscopic properties also for very low mass stars. In our simulations, LTE models are used both for the quiet photosphere and the active regions (spots and faculae). NLTE models from Fontenla et al. (2009) will be considered in future versions of the code to model faculae, as they have shown to better reproduce the spectral irradiance of activity features over all the magnetic cycle in the case of the Sun (Fontenla et al. 2011). Synthetic spectra from BT-Settl models are available for 2600 K $< T_{\rm eff} <$ 70000 K, +3.5 $\leq \log g \leq$ +5.0 and several values of alpha enhancement and metallicity. An example for a solar-type star is shown in Fig. 1.

These models include the effects of convection as described by the mixing length theory of turbulent transport (Vitense 1953) characterized by the mixing length parameter α as discussed by Ludwig et al. (1999) using 3D radiative models. Convection has a significant impact on line profiles, which are modified when active regions cross the stellar surface, and hence it is responsible for a significant part of the jitter observed in RV measurements (Meunier et al. 2010a).

A BT-Settl database of spectra is currently available for resolutions defined by a sampling ≥0.05Å, which is not enough to study line profiles and obtain accurate RV measurements. In or-

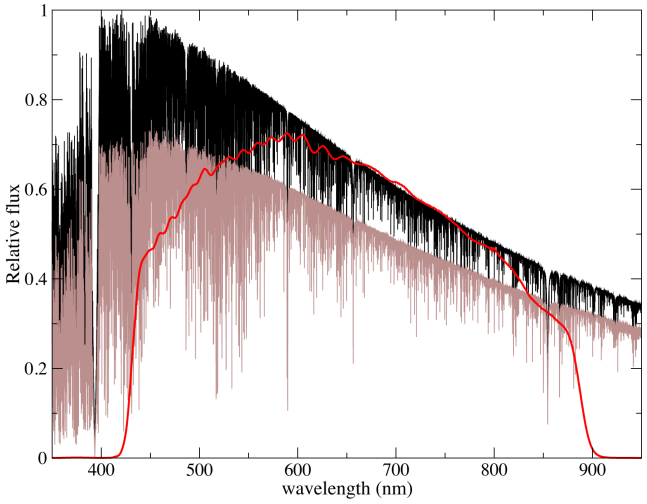

Fig. 1. Solar-like star synthetic spectrum for $T_{\rm eff}$ =5770 K and $\log g$ = 4.5 (black) generated with BT-Settl models, compared to a synthetic spectrum with a $T_{\rm eff}$ value 310 K lower (brown), which could be representative of a spot. In red, the transmission function of the Kepler passband.

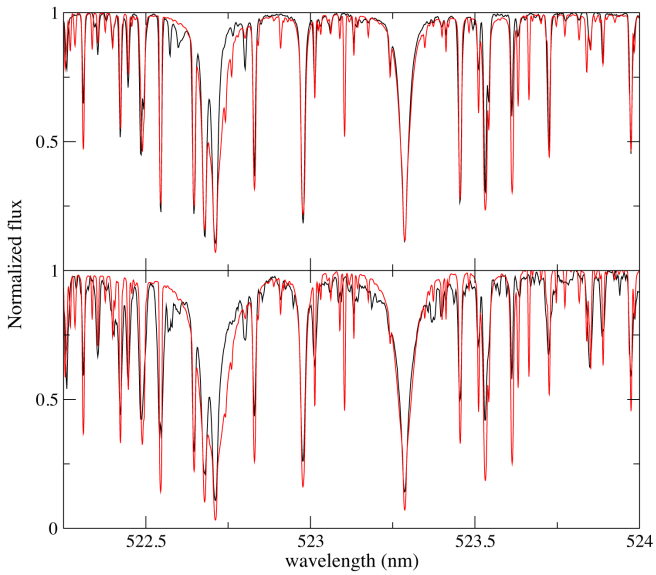

Fig. 2. Top: Comparison between an observed high-resolution spectrum for the solar photosphere (black) and a Phoenix synthetic spectrum (red) from Husser et al. (2013) using $T_{\rm eff}$ =5770 K, $\log g$ = 4.5 and solar abundances. Bottom: Same for the observed spectrum of a spot region (black), now compared with a Phoenix synthetic spectrum of $T_{\rm eff}$ =5460 K.

der to perform simulations for RV jitter studies and line profiles, high resolution spectra presented by Husser et al. (2013) are used instead. The library is also based on the Phoenix code, and the synthetic spectra cover the wavelength range from 500 to 5500 nm with resolutions of $R = 500,000$ in the optical and near IR, $R = 100,000$ in the IR and $\Delta\lambda = 0.1$Å in the UV. The parameter space covers 2300 K $\leq T_{\rm eff} \leq$ 12000 K, 0.0 $\leq \log g \leq$ +6.0, -4.0 $\leq$ [Fe/H] $\leq$ +1.0, and 0.2 $\leq [\alpha/{\rm Fe}] \leq$ +1.2.

2.1.2. Solar spectra

In addition to synthetic spectra from model atmospheres, observed high-resolution spectra of the Sun are used in order to test the results coming from the Phoenix models. The spectra are obtained from a photospheric region and a spot with the 1-meter Fourier Transform Spectrometer of the National Solar Observatory located at Kitt Peak, and have a resolution of $R \sim 10^6$ covering wavelengths from 390 nm to 665 nm. Figure 2 shows a comparison between the solar observed spectra and synthetic Phoenix spectra from Husser et al. (2013) for a Sun-like star, both for the quiet photosphere and for a spot region. The temperature of the photospheric region was fixed to $T_{\rm eff}$ =5770 K for the synthetic spectrum, which agrees with most of the features in the observed data. In the case of the spot spectrum, $T_{\rm eff}$ was varied from 4500 to 5500 K, finding the best agreement for 5460 K (temperature contrast $\Delta T_{\rm spot}$=310 K) when considering the whole wavelength range. This was done by minimizing the rms of the different models divided by the spectrum of the spot. The result is consistent with the measurements made by Eker et al. (2003), who determined $\Delta T_{\rm spot} \simeq$300 K for the combination of umbra and penumbra by analysing multi-channel fluxes of an equatorial passage of a sunspot.

2.2. Data simulation

2.2.1. Model and stellar parameters

The stellar photosphere is divided into a grid of surface elements whose physical and geometrical properties are described individually. The space resolution of the grid is an input parameter of the program, and $1^\circ \times 1^\circ$ size elements have been found to be adequate to correctly reproduce most active region configurations and transiting planet effects down to $\sim 10^{-6}$ photometric precision. A complete list of the input parameters of the program is presented in Table 1. The table also shows the typical values considered for each parameter, based on the grid coverage of the models and on some physical constraints that are discussed below.

The `StarSim` tool is able to reproduce any possible distribution of active regions that can be defined with the adopted surface grid. Active regions with complex geometric properties can be defined by adding the contribution of small circular ones. The total number of active regions, as well as their surface and time distributions, can be provided as an input by the user or randomly generated by the program following different statistics defined in the input parameters. The number of regions at a given time depends on a flat distribution between a specified minimum, $Nr_{\rm min}$, and a maximum, $Nr_{\rm max}$. The sizes of the spots follow a Gaussian distribution, defined by a mean area $\bar{A}_{\rm Sn}$ and a standard deviation $\sigma(A_{\rm Sn})$, in units of the total stellar surface. Therefore, the mean filling factor ($\bar{FF}$) over time in the whole stellar surface is determined by the mean number of spots, $\bar{Nr} = (Nr_{\rm max} + Nr_{\rm min})/2$ and their mean area by:

$$\bar{FF} = \bar{Nr} \cdot \bar{A}_{\rm Sn} \quad (1)$$

Note that this filling factor only varies due to active region evolution and is different from the projected filling factor, which

also accounts for the geometric projection of spots due to stellar inclination and rotation modulation.

Although the geometric description of the spots is free (only defined by the properties of the underlying stellar grid), tests have been carried out by modelling each active region n as a circular spot of radius $R_{\rm Sn}$ surrounded by a corona associated to a facular region, having an external radius $R_{\rm Fn} = \sqrt{Q+1} \cdot R_{\rm Sn}$ (see Fig. 3), where Q is the ratio between the area of the surrounding faculae and the area of the spot, which is assumed to be the same for all the active regions on the star. Our model does not distinguish between spot umbra and penumbra, but adopts a mean spot contrast at an intermediate temperature, similar to the prescription used by previous approaches (Chapman 1987; Unruh et al. 1999). The model of circular spots surrounded by a corona of faculae has been shown to successfully reproduce spot maps for the Sun (Lanza et al. 2003) and for several low mass stars with high precision light curves (Lanza et al. 2009, 2010; Silva-Valio et al. 2010). Solar observations have shown the presence of systematic changes in the contrast and size of faculae (Chapman 1987), with the value Q decreasing for larger active regions that are more frequent around the maximum of activity (Chapman et al. 2011). Foukal (1998) shows that the relationship between the area of the faculae and the area of the spots is not linear, and can vary from $Q \sim 2$ to $Q \sim 10$ depending on the size and lifetime of the active regions. In our case, we choose values from $Q \sim 3$ to $Q \sim 8$, representing medium- and small-sized spots for the simulations of Sun-like star data. Several studies on the modelling of high precision light curves conclude that lower values of Q or even $Q = 0$ (i.e., no faculae) provide the best description of the data for K and early M dwarfs (Gondoin 2008; Lanza et al. 2010, 2011b). In our work we investigate and discuss the appropriate presence of faculae to be included in the simulations of each particular case.

The geometric distribution of the active regions is not constrained in the `StarSim` tool, so this can be either user defined or generated randomly. In the second case, the longitudes of the active regions are equally distributed over the stellar surface, whereas the latitudes are distributed in two belts defined by Gaussian functions centered at $\pm\bar{\theta}_{\rm belt}$. This configuration can be used in order to simulate butterfly diagram evolution patterns, which are well known for the Sun (Jiang et al. 2011; Vecchio et al. 2012) and several active dwarfs (Katsova et al. 2003; Berdyugina & Henry 2007; Livshits et al. 2003), together with other long term variations (Pulkkinen et al. 1999). Latitudes of spots have also been measured for several stars from observations of spot crossing events (Sanchis-Ojeda & Winn 2011).

Active region evolution can also be modelled with `StarSim`. This is done by considering a linear increase of the spot sizes with time, followed by a time interval of constant size and a final decay. In the case of selecting a random distribution of the parameters of the active regions, the total typical lifetime of active regions, $\bar{L}_{\rm n}$, its standard deviation, $\sigma(L_{\rm n})$, and the growing/decaying rate, $a_{\rm rd}$, are also specified when configuring the simulation. Spots are known to live for weeks on main sequence stars, and months in the case of locked binary systems (Hussain 2002; Strassmeier et al. 1994a,b). However, polar starspots have been observed to last for years (Olah & Pettersen 1991). Measurements of the decay rate of sunspots have shown that it follows a parabolic area decay law (Petrovay & van Driel-Gesztelyi 1997; Petrovay et al. 1999) although previous studies assumed both linear and non-linear laws (Martinez Pillet et al. 1993). Regarding other stars, Doppler imaging observations of isolated starspots over time are not yet available in high resolution. In the case of our simulations, a parabolic law is considered, both for the decay and for the emergence of the active regions, and the evolution rate is set to the solar values except for stars where the surface map has been modelled for a long enough time span to estimate spots lifetimes and observe variations in size.

Note that, in the current implementation, our simulator is not intended to model each active region as a group of small spots, but to consider it as a single circular spot. We assume that this approach, by considering the appropriate size and evolution of the active regions, generates mostly the same effects on the simulated photometric and spectroscopic data as using a more complicated group-pattern configuration. In our simulations, we adjust the number and size of active regions to be in agreement with the results from the literature that assume a two-temperature structure (Henry et al. 1995; Rodonò et al. 2000; Padmakar & Pandey 1999). Solanki & Unruh (2004) discuss the distribution of spot sizes for some Sun-like stars observed with the Doppler imaging technique. Although it is suggested that sizes could follow a lognormal distribution as on the Sun, we do not adopt such distribution because the smaller spots would not cause a significant effect on our simulations compared to large spots, especially for the most active stars where large spots dominate (Solanki & Unruh 2004; Jackson & Jeffries 2013; Strassmeier 2009).

Spot temperatures have only been determined in a few cases, and the inhomogeneity of the results due to the diversity of techniques make this still an unconstrained parameter. Most of the current measurements made in main sequence stars come from Doppler imaging (Marsden et al. 2005; Strassmeier & Rice 1998) or multi-band light curve modelling (Petrov et al. 1994; O'Neal et al. 2004). The first ones are limited to young fast-rotating active stars that can present a different kind of activity pattern (Mullan & MacDonald 2001), and it is not clear that these results can be extrapolated to the active regions in Sun-like stars. Berdyugina (2005) showed that, on average, the spot temperature contrast $\Delta T_{\rm spot}$ has a dependence on the spectral type, being larger for hotter stars. However, there seems to be no correlation between spot temperatures and sizes (Bouvier & Bertout 1989; Strassmeier 1992) or activity cycles (Stix 2002; Albregtsen & Maltby 1981; Penn & MacDonald 2007) in the case of the Sun. In our simulations we assume the same $\Delta T_{\rm spot}$ for all the active regions, which is estimated from a low order polynomial fit to the data in Berdyugina (2005),

$$\Delta T_{\rm spot} = 7.9 \cdot 10^{-5} T_{\rm eff} - 0.1056 T_{\rm eff} - 153.6. \quad (2)$$

This is consistent with the temperature measurements of the darkest regions of the spot in the case of the Sun (Eker et al. 2003). When possible, we use more accurate determinations of the whole spot region properties based on their spectral signature (see Sect. 3; also Pont et al. 2008, 2013; Sing et al. 2011).

As explained in Sect. 2.1.1, Phoenix models are used to reproduce the spectral signature of faculae in our approach. Faculae are known to be mainly a magnetic phenomenon affecting the intensity of the spectral lines, best reproduced by NLTE simulations (Carlsson & Stein 1992). The lack of high resolution models for faculae in the spectral range of our interest prevents us from including them into high resolution spectra simulations, restricting them to the simulations of broad band photometric variations (see Sect. 2.2.2). A positive temperature contrast between the faculae and the photosphere, $\Delta T_{\rm fac} \simeq 30 - 50$ K is assumed, as reported by Badalyan & Prudkovskii (1973) from observations of the CO line in faculae and by Livshits & Polonskii (1968) from a more theoretical point of view. Solanki (1993) provides an extensive discussion and references on the weaken-

Table 1. Input parameters

Parameter	Typical values
Initial time of simulation (days)	–
Final time of simulation (days)	–
Data time cadence (minutes)	–
Working mode	Phot. / Spec.
Spectral range (nm)	500 – 50000
Photometric filter	–
Grid resolution (°)	$1° \times 1°$
RV window of the CCF, $\Delta v_{\rm CCF}$ (km s^{-1})	20 – 40
Add photon noise	y/n
Stellar apparent magnitude K	–
Telescope area (m^2)	–
Instrument efficiency	0 – 1
$T_{\rm eff}$ (K)	2600 – 12000
$\log g$	+3.5 – +5.0
[Fe/H]	−4.0 – +1.0
[α/Fe]	0.2 – +1.2
Spots temperature contrast, $\Delta T_{\rm spot}$ (K)	200 – 1500
Faculae temperature contrast, $\Delta T_{\rm fac}$ (K)	30 – 50
Facula-to-spot area ratio, Q	0.0 – 10.0
Stellar rotation period, P_0 (days)	–
Differential rotation, $k_{\rm rot}$	–
Inclination angle, i_* (°)	0 – 90°
Minimum number of spots, Nr_{min}	–
Maximum number of spots Nr_{max}	–
Mean area of spots $\bar{A}_{\rm Sn}$	–
Standard deviation of the area of spots $\sigma(A_{\rm Sn})$	–
Mean lifetime of active regions, $\bar{L}_{\rm n}$ (days)	10^1-10^3
Standard deviation of lifetime of active regions $\sigma(L_{\rm n})$ (days)	–
Growing/decaying rate $a_{\rm rd}$ (°/day)	–
Mean latitude of active regions $\pm\bar{\theta}_{\rm belt}$ (°)	0 – 90°
Standard deviation of latitude of active regions $\sigma(\theta_{\rm belt})$ (°)	0 – 90°
Planet radius, $R_{\rm planet}/R_*$	–
Mid transit time, T_0 (days)	–
Orbital Period, $P_{\rm planet}$ (days)	–
Impact parameter, b	0 – 1
Spin-orbit angle, γ (°)	0 – 90°

ing of lines in faculae and the needed $\Delta T_{\rm fac}$ to best reproduce the continuum brightness.

A transiting planet can also be introduced in the simulations to investigate activity effects on photometric and radial velocity observations during transits. The planet is modelled as a circular black disk and is described in the same way as a spot with zero flux, but assuming a circular projection on the stellar disk. No planetary atmosphere is considered in the current implementation and so the radius of the planet has no wavelength dependence. The photometric signal for the primary transit is generated from the planet size, the ephemeris and the orbit orientation (inclination and spin-orbit angles), which are specified as input parameters. The orbital semi-major axis is computed from the orbital period, $P_{\rm planet}$, and the stellar mass, M_*, using Kepler's Third Law by assuming $M_* \gg m_{\rm planet}$. Eccentricity is considered to be zero for all cases in the current model.

Together with the physical parameters of the star-planet system, the spectral range for the output data, the timespan of the simulations and the cadence of the data series can be selected. The program generates the resulting time series spectra and also creates a light curve by multiplying each generated spectrum by a filter passband specified from a database. If preferred, a filter with a rectangular transfer function can be defined and used to study the photometric signal at any desired wavelength range. Finally, the integration time, the telescope collecting area, the efficiency of the instrument and the target star magnitude are needed to apply photon noise statistics to the resulting fluxes.

2.2.2. Simulating photometric time series

To build the spectrum of the spotted stellar surface, three initial synthetic spectra generated from models with different temperatures are computed for the quiet photosphere, spots and faculae. The program reads the physical parameters for the three photospheric features of the modelled star and interpolates in $T_{\rm eff}$ within the corresponding model grids to generate the three synthetic spectra: $f_p(\lambda)$, $f_s(\lambda)$ and $f_f(\lambda)$. The rest of the stellar parameters (i.e. $\log g$, metallicity, etc.) are not significantly variable over the stellar surface, and specifically not for active regions. Therefore, their precision is not critical for the purpose of our simulations, and the nearest grid values are considered instead of interpolations.

Kurucz (ATLAS9) spectra are computed for the specified parameters reproducing the photosphere and the spots. These models provide information on the intensity profile of the star, which can be used in order to compute the limb darkening factors, $I(\lambda,\mu)/I(\lambda,0)$. With our approach, such a factor is computed separately for every surface element and wavelength. This is done by interpolating within the grid of intensities provided by the Kurucz models. Then, the spectrum of the undarkened surface element ($f_p(\lambda)$ for the quiet photosphere or $f_s(\lambda)$ for the spots) is multiplied by the corresponding limb darkening factor, $I_p(\lambda,\mu)/I_p(\lambda,0)$ or $I_s(\lambda,\mu)/I_s(\lambda,0)$ (see Eqs. 4, 10, 14). In the case of faculae, a different approach is considered, as it is known that these areas are brightened near the limb (Frazier & Stenflo 1978; Berger et al. 2007). A limb brightening law is considered in this case, as presented in Eq. 13.

The code produces time series data considering the initial and final times and the cadence of the time series specified in the input parameters. For each time step, the evolutionary stage (current size) and the projected position of each active region are computed. This last parameter is obtained from the specified rotation period, P_0, and the differential rotation of the star, which is modelled as described by Beck (2000):

$$\Omega(\theta) = \Omega_0 + k_{\rm rot}(\Omega_{\odot \rm A} \cdot \cos^2\theta + \Omega_{\odot \rm B} \cdot \cos^4\theta), \quad (3)$$

where Ω_0 is the equatorial rate, $\Omega_{\odot \rm A} = 1.698°{\rm day}^{-1}$ and $\Omega_{\odot \rm B} = 2.346°{\rm day}^{-1}$ are the coefficients that describe the differential rotation for the Sun (Snodgrass & Ulrich 1990), $k_{\rm rot}$ is a factor that sets the differential rotation rate for the star and is specified in the input parameters (the value for the Sun would be $k_{\rm rot}$=1), and θ is the colatitude.

In a first step, the spectrum for the quiet photosphere is obtained from the contribution of all the surface elements, taking into account the geometry of the element, its projection towards the observer, the corresponding limb darkening profile and the RV shift:

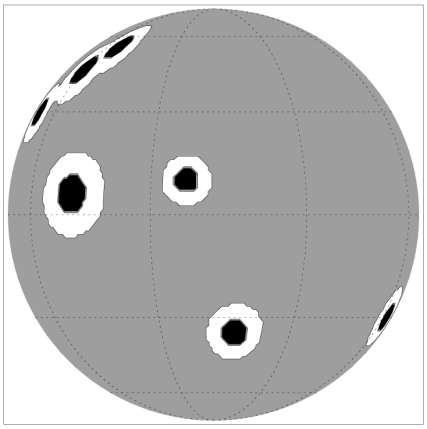

Fig. 3. Projected map for an arbitrary distribution of active regions with $Q = 3.0$. The quiet photosphere is represented in grey, and each active region is modelled as a cold spot (black) and a hotter surrounding area associated with faculae (white).

$$f_{im}(\lambda) = \sum_k f_p(\lambda_k, \mu_k, a_k) = \\ = \sum_k f_p(\lambda_k) \cdot \frac{I_p(\lambda_k, \mu_k)}{I_p(\lambda_k, 0)} \cdot a_k \cdot \mu_k \cdot \omega_k, \quad (4)$$

where k is the surface element and μ_k is the cosine of its projection angle given by

$$\mu_k = \sin i_* \sin\theta_k \cos\phi_k + \cos i_* \cos\theta_k, \quad (5)$$

where θ_k and ϕ_k are the colatitude and longitude coordinates, respectively, and i_* is the stellar axis inclination.

The factor ω_k accounts for the visibility of the surface element and is given by

$$\omega_k = \begin{cases} 1 & \text{if } \mu_k \geq 0 \\ 0 & \text{if } \mu_k < 0, \end{cases} \quad (6)$$

and a_k is the area of the surface element, which can be computed from the spatial resolution of the grid ($\Delta\alpha$) by

$$a_k = 2 \cdot \Delta\alpha \cdot \sin(\frac{\Delta\alpha}{2}) \sin\theta_k. \quad (7)$$

Finally, λ_k are the wavelengths including the Doppler shift for the corresponding surface element,

$$\lambda_k = \lambda + \Delta\lambda_k, \quad (8)$$

with

$$\Delta\lambda_k \simeq -8.05 \cdot \lambda \cdot \frac{1}{c} \cdot R_{\rm star} \cdot \frac{2\pi}{P_0} \sin i_* \sin\theta_k \sin\phi_k. \quad (9)$$

These are computed from the equatorial rotation period given in the input parameters and the stellar radius calculated using its relation with $\log g$ and $T_{\rm eff}$ for main sequence stars.

The flux variations produced by the visible active regions are added to the contribution of the immaculate photosphere when computing the spectrum at each time step j. These are given by

$$\Delta f_j^{ar}(\lambda) = \\ = \sum_k [(f_s(\lambda_k) \cdot J_s^{kj}(\lambda_k) - f_p(\lambda_k) \cdot J_p^{kj}(\lambda_k)) \cdot p_s^{kj} + \\ + (f_f(\lambda_k) \cdot J_f^{kj} - f_p(\lambda_k) \cdot J_p^{kj}(\lambda_k)) \cdot p_f^{kj}], \quad (10)$$

where the first term accounts for the flux deficit produced by the spots and the second is the overflux produced by faculae. The quantities $J_p^{kj}(\lambda_k)$, $J_s^{kj}(\lambda_k)$ and J_f^{kj} account for the geometric and the limb darkening/brightening factors for the surface element k at the time step j of the simulation, and are given by:

$$J_p^{kj}(\lambda_k) = \frac{I_p(\lambda_k, \mu_{kj})}{I_p(\lambda_k, 0)} \cdot a_k \cdot \mu_{kj} \cdot \omega_{kj} \\ J_s^{kj}(\lambda_k) = \frac{I_s(\lambda_k, \mu_{kj})}{I_s(\lambda_k, 0)} \cdot a_k \cdot \mu_{kj} \cdot \omega_{kj} \\ J_f^{kj} = c_{\rm f}(\mu_{kj}) \cdot a_k \cdot \mu_{kj} \cdot \omega_{kj}. \quad (11)$$

The factors p_s^{kj} and p_f^{kj} are the fractions of the surface element k covered by spot and faculae, respectively. These amounts are computed for every surface element considering their distance to the center of all the neighbour active regions at each observation j. There is also a time dependence of the projection of the surface elements, given by

$$\mu_{kj} = \sin i_* \sin\theta_k \cos[\phi_k + \Omega(\theta) \cdot (t_j - t_0)] + \cos i_* \cos\theta_k. \quad (12)$$

Finally, $c_f(\mu_{kj})$ accounts for the limb brightening of faculae, which is assumed to follow the law used by Meunier et al. (2010a):

$$c_{\rm f}(\mu_{kj}) = \left(\frac{T_{\rm eff} + \Delta T_\mu(\mu_k)}{T_{\rm eff} + \Delta T_{\rm fac}} \right)^4, \quad (13)$$

where $\Delta T_\mu(\mu) = a_\mu + b_\mu \cdot \mu_k + c_\mu \cdot \mu_k^2$.

The coefficients are $a_\mu = 250.9$, $b_\mu = -407.4$ and $c_\mu = 190.9$, so that $c_{\rm f}(\mu_{kj}) \sim 1$ at the center of the disk and ~ 1.16 near the limb for a Sun-like star with $\Delta T_{\rm fac} = 30$ K. This is in agreement with the parametrizations presented by Unruh et al. (1999). The observations show that the contribution of faculae dominate the irradiance in the case of the Sun, where active regions are ∼1.2 times brighter at the limb than at the center of the stellar disk (Ortiz et al. 2002; Ball et al. 2011; Steinegger et al. 1996).

As explained in Sect. 2.2.1, a transiting planet can be included as a dark circular spot with a constant radius over wavelength (no atmosphere) crossing the stellar disk. For each time step j, the planet position is obtained from the given ephemeris and the flux deficit is computed from the eclipsed surface elements of the star:

$$\Delta f_j^{tr}(\lambda) = -\sum_k f_p(\lambda_k) \cdot J_p^{kj}(\lambda_k) \cdot p_{tr}^{kj}, \quad (14)$$

where p_{tr}^{kj} is the fraction of the surface element k covered by the planet at time step j. In case an active region is partially

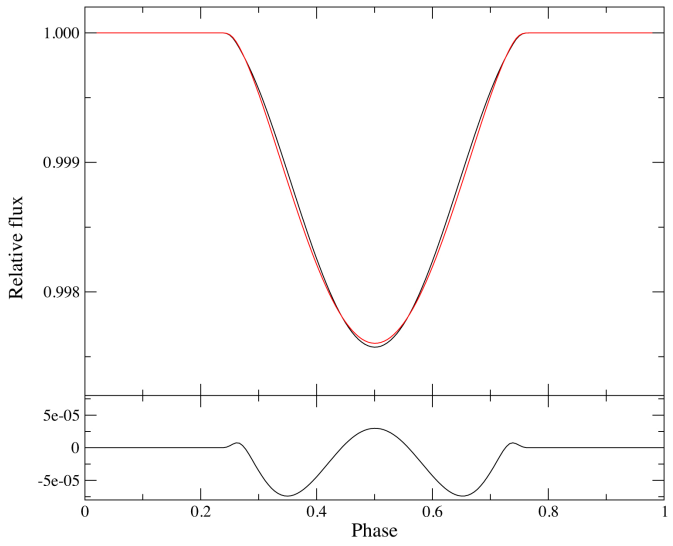

Fig. 4. Top panel: A comparison between two light curves obtained for a star with $T_{\rm eff}$ = 5777 K, log g = 4.5 and $\Delta T_{\rm spot}$ = 320 K from Phoenix BT-Settl models (red) and solar observed spectra (black), by introducing an equatorial spot covering ∼ 0.3% of the visible stellar surface. Bottom panel: The difference between both light curves.

occulted by the planet, the corresponding spot (p_s^{kj}) and facula (p_f^{kj}) fractions (see Eq. 10) in the occulted surface elements are computed within the planet covered fraction (p_{tr}^{kj}) instead.

Finally, the spectrum for the observation j is obtained by adding the contribution of the immaculate photosphere, the active regions and the transiting planet:

$$f_j(\lambda) = f^{im}(\lambda) + \Delta f_j^{ar}(\lambda) + \Delta f_j^{tr}(\lambda). \quad (15)$$

When working with the low resolution Phoenix spectra to produce a photometric time series, the resulting spectra are multiplied by the specified filter passband (see Fig.1) to obtain the total flux and to compute the jitter produced by activity at the desired spectral range. The photometric jitter is evaluated by computing the rms of the flux over time for the whole photometric data series.

A comparison between two light curves obtained from Phoenix models and solar observed spectra for the Johnson-V band is presented in Fig. 4. The simulation covers one rotation period of a Sun-like star with a single circular spot and no faculae. The spot is located on the equator and covers ∼ 0.3% of the visible stellar surface. The temperature contrast of the spot, $\Delta T_{\rm spot}$, was fitted considering 10 K steps in the Phoenix spectrum of the spot and minimizing the rms of the residuals between both light curves. The best solution was found for $\Delta T_{\rm spot}$ = 320 K, presenting differences at the 10^{-5} level, which is in close agreement with the contrast found by direct determination from the spectra (see Sect. 2.1.2). We conclude that the small deviations shown by the models for specific spectral lines do not have a significant impact at the required photometric level when considering broad spectral bands.

The position of the photocenter on the stellar disk is also computed for each time step j of the simulations. This is implemented for a further investigation of the astrometric jitter caused by the presence of active regions or transiting planets. The astrometric shifts depend on wavelength and are computed separately for the equatorial axis (X) and the spin projected axis of the star (Y) by:

$$\begin{aligned}\Delta X^j(\lambda) = \sum_k \{ & f_p(\lambda_k)\cdot J_p^{kj}(\lambda_k)\cdot x_{kj} + \\ & + [f_s(\lambda_k)\cdot J_s^{kj}(\lambda_k) - f_p(\lambda_k)\cdot J_p^{kj}(\lambda_k)]\cdot p_s^{kj}\cdot x_{kj} + \\ & + [f_f(\lambda_k)\cdot J_f^{kj} - f_p(\lambda_k)\cdot J_p^{kj}(\lambda_k)]\cdot p_f^{kj}\cdot x_{kj} + \\ & + f_p(\lambda_k)\cdot J_p^{kj}(\lambda_k)\cdot p_{tr}^{kj}\cdot x_{kj}\} \end{aligned} \quad (16)$$

and

$$\begin{aligned}\Delta Y^j(\lambda) = \sum_k \{ & f_p(\lambda_k)\cdot J_p^{kj}(\lambda_k)\cdot y_{kj} + \\ & + [f_s(\lambda_k)\cdot J_s^{kj}(\lambda_k) - f_p(\lambda_k)\cdot J_p^{kj}(\lambda_k)]\cdot p_s^{kj}\cdot y_{kj} + \\ & + [f_f(\lambda_k)\cdot J_f^{kj} - f_p(\lambda_k)\cdot J_p^{kj}(\lambda_k)]\cdot p_f^{kj}\cdot y_{kj} + \\ & + f_p(\lambda_k)\cdot J_p^{kj}(\lambda_k)\cdot p_{tr}^{kj}\cdot y_{kj}\}, \end{aligned} \quad (17)$$

where the quantities $J_p^{kj}(\lambda)$, $J_s^{kj}(\lambda)$ and $J_f^{kj}(\lambda)$ are given by Eq. 11 and x_{kj} and y_{kj} denote the position of the surface element k projected on the X and Y axes, respectively, at the time step j of the simulation. The rest of the variables are defined in Eqs. 4 to 14.

The first term in Eqs. 16 and 17 provides the position of the photocenter for an immaculate photosphere, whereas the second, third and fourth add the contribution of spots, faculae and planet to the astrometric shifts. As in Eq. 14, the corresponding flux contribution is computed within p_{tr}^{kj} and subtracted from p_s^{kj} or p_f^{kj}, when the planet is occulting a surface element k containing a spot or a facula, respectively.

$\Delta X^j(\lambda)$ and $\Delta Y^j(\lambda)$ vectors are finally multiplied by a given instrumental response function or a filter passband to produce astrometry displacement curves. Two simple cases are presented in Fig. 5 for a Sun-like and a K0-type star observed at $i = 90°$. A single circular active region was considered, consisting of a spot of size $A_{\rm Sn} = 1.6\cdot 10^{-3}$ relative to the stellar surface and a surrounding facular area with Q = 3.0, located on the equator of the star ($\theta = 90°$). The temperature contrast of the spot was set to $\Delta T_{\rm spot}$ = 310 K for the Sun-like star and $\Delta T_{\rm spot}$ = 250 K for the K0 star (see Sect. 2.2.1 and Berdyugina 2005). The photometric signature can be seen in the top panel, which is dominated by faculae when the active region appears at the edges of the stellar disk (phases ∼ 0.3 and ∼ 0.7) as an effect of limb brightening, while the dark spot produces a decrease of ∼ 0.001 in relative flux units at the center of the stellar disk (phase∼0.5). The astrometric signature (middle panel) peaks at $\pm 0.001 R_*$. This jitter would only affect astrometric measurements at the expected precision of the Gaia space mission (Lindegren et al. 2008; Eyer et al. 2013) for main sequence stars located at 20 pc or closer. Further analysis and discussion on astrometric jitter simulations will be presented in a future paper.

2.2.3. Simulating spectroscopic data

A similar methodology as the one presented in Sect. 2.2.2 is implemented for the simulation of time series data to obtain activity-induced RV curves. A drawback of the methodology used is the large volume of data produced when working with high-resolution spectra, which is solved by working in the velocity space, as explained below.

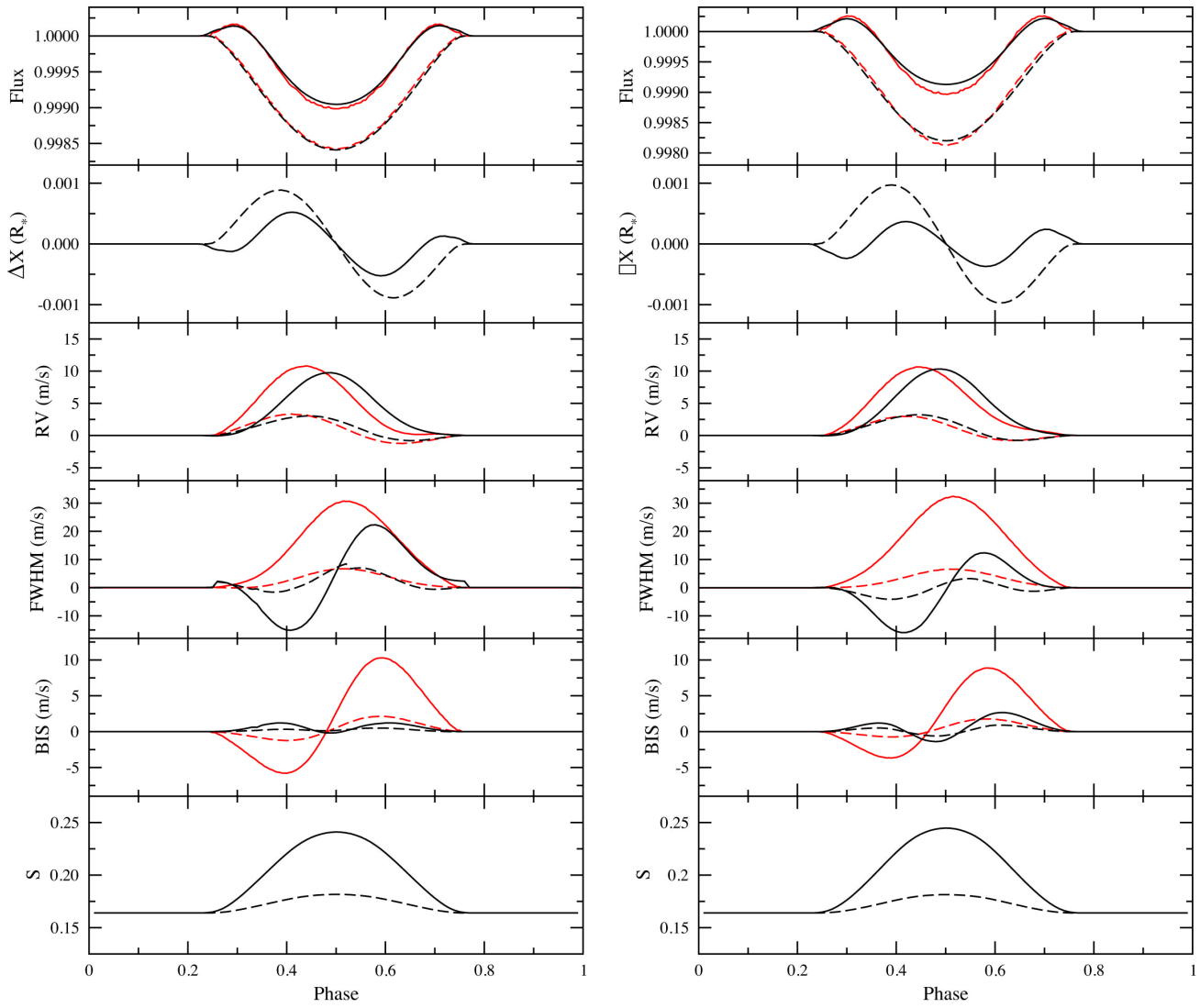

Fig. 5. Simulations of an active region located on the equator $\theta = 90°$ with a size of $A_{\rm Sn} = 1.6 \cdot 10^{-3}$ relative to the stellar surface. The rotation period is 25 days and the inclination is 90°, yielding $v \sin i = 2$ km s^{-1}. Left panels: simulated data for a Sun-like star ($T_{\rm eff} = 5770$ K) and $\Delta T_{\rm spot} = 310$ K. Right panels: the same for a K0 star ($T_{\rm eff} = 5000$ K) and $\Delta T_{\rm spot} = 250$ K. From top to bottom: photometric (in Johnson V band), astrometric, RV, FWHM, BIS and S index variations induced by the active region. The results with surrounding faculae ($Q = 3$) are shown with black solid lines and the ones with no faculae ($Q = 0$) are plotted with black dashed lines. The same simulations made with SOAP 2.0 are plotted with red lines.

Three synthetic spectra ($f_p(\lambda)$, $f_s(\lambda)$ and $f_f(\lambda)$) for the given wavelength range are computed for different temperatures corresponding to the quiet photosphere, spots and faculae, by interpolating from Husser et al. (2013) Phoenix library (see Sect. 2.1.1). The nearest values in the grid to the specified ones are considered for the rest of the parameters, as done in Sect. 2.2.2. Then, individual CCFs ($C_p(v), C_s(v)$ and $C_f(v)$) are computed, respectively, from the three spectra and a template mask consisting of a synthetic spectrum of a slowly rotating inactive star of the same parameters. In the current version of `StarSim`, the mask templates from the HARPS instrument pipeline (DRS,Cosentino et al. 2012) are used in order to compute the CCFs contribution of the different elements (Pepe et al. 2002, 2004). These are optimized for G2, K5 and M2 type main sequence stars and consist on a selection of delta-peak lines, whose height corresponds to the line equivalent width.

The global CCF of the projected stellar surface is computed from the contribution of the individual surface elements. First, the signature of the immaculate photosphere is obtained from

$$C^{im}(v) = \sum_k C_p(v_k, \mu_k, a_k) = \sum_k C_p(v_k) \cdot H_p^k, \tag{18}$$

where the quantity H_p^k accounts for the intensity and geometric factors of the surface element k,

$$H_p^k = \sum_\lambda f_p(\lambda) \cdot \frac{I_p(\lambda, \mu_k)}{I_p(\lambda, 0)} \cdot a_k \cdot \mu_k \cdot \omega_k. \tag{19}$$

The summation covers the whole wavelength range specified for $f_p(\lambda)$.

The shifted velocities, v_k, are computed from the contribution of the Doppler shift and the effects of convection,

$$v_k = v + \Delta v_k^{\rm DS} + \Delta v_k^{\rm C}(C_l), \tag{20}$$

for $l = \{p, s, f\}$, where $\Delta v_k^{\rm DS}$ is the contribution from the Doppler shift for the surface element k (see Eq. 9) and $\Delta v_k^{\rm C}(C_i(v))$ is the effect of convective blueshift, which depends on the line depth and can be characterized by studying the line bisectors, which will typically show a distinctive C-shape due to granulation in the photosphere (Gray 1992).

Note that the effects of convection in the line profile are included in the Phoenix spectra from Husser et al. (2013) (see Sect. 2.1) assuming a surface element in LTE observed at $\mu = 1$. However, this description is too simple and only valid for surface elements located at the center of the stellar disk. Therefore, we decided to employ a more sophisticated treatment introducing the convective blueshift from CIFIST 3D models (Ludwig et al. 2009) including NLTE effects. The convection effects of the Phoenix spectra are fitted with a low order polynomial function to the CCF computed with the full spectral range, and then subtracted. Next, we add the convective blueshift contribution computed from the 3D models. They are available for a Sun-like star and several projection angles ranging from the disk center to the stellar limb (C. Allende Prieto, private communication). We computed the CCFs and then fitted low order polynomial functions to the line bisectors for the different available projection angles. Then, we obtained the $\Delta v_k^{\rm C}(C_p)$, $\Delta v_k^{\rm C}(C_s)$ and $\Delta v_k^{\rm C}(C_f)$ for any projection angle μ_k from a linear interpolation of the available models. In the case of the active regions (i.e., both spot and facula zones), where convection is known to be blocked by strong magnetic fields (see Strassmeier 2009 and references therein), the solar high-resolution observed spectra described in Sect. 2.1.2 are used in order to compute the shift in the line bisector with respect to the photosphere. This is then scaled with μ and added to the amounts $\Delta v_k^{\rm C}(C_s)$ and $\Delta v_k^{\rm C}(C_f)$ of the surface elements where a contribution of spot or faculae is present. In this way, the contribution of active regions is redshifted ~ 0.3 km s^{-1} (see Fig. 6) due to the inhibition of convection (Dumusque et al. 2014).

Figure 6 shows four of the bisectors computed by using the full HARPS wavelength range (~380 - 670 nm) from CIFIST 3D model spectra and by using the solar observed spectra for a quiet Sun region and a spot. The right panel also shows a comparison with the bisectors of 18 Sco and α Cen A, which have very similar physical properties as the Sun and were observed with HARPS at a minimum activity level (X. Dumusque, priv. comm.). They are displayed together with the simulation of the bisector of a spotless photosphere of a Sun-like star generated with `StarSim`. The differences are below ~10-20 m s^{-1} and <10 m s^{-1} for contrasts <0.9, so that the simulated bisectors reproduce the general behavior of the HARPS observations. The differences at the top of the bisector could be due to deviations from the real limb darkening profile, i.e. having more weight at the stellar disk center would increase the effect of C-shaped lines. Also, more accurate modelling of convection effects on shallow lines would be needed in order to improve the agreement on this part of the bisector.

The vertical component of the convective velocity produces a maximum shift at the center of the stellar disk, while the effect is barely seen near the limb where the projected velocity is zero. On the other hand, an apparent redshift of the spectral lines in comparison to the quiet photosphere is observed in spotted and facular areas as convective motions are blocked (Meunier et al. 2010b). Therefore, convection effects will introduce a maximum shift in RV measurements when a dark spot is crossing the center of the stellar disk.

The variations produced by active regions on the observed CCF at each time step j of the simulation are given by

$$\begin{aligned}\Delta C_j^{ar}(v) &= \\ &= \sum_k \{[C_s(v_k)\cdot H_s^{kj} - C_p(v_k)\cdot H_p^{kj}]\cdot p_s^{kj} + \\ &+ [C_f(v_k)\cdot H_f^{kj} - C_p(v_k)\cdot H_p^{kj}]\cdot p_f^{kj}\},\end{aligned} \tag{21}$$

where the quantities H_p^k, H_s^k and H_f^k are computed by

$$\begin{aligned}H_p^{kj} &= \sum_\lambda f_p(\lambda)\cdot\frac{I_p(\lambda,\mu_{kj})}{I_p(\lambda,0)}\cdot a_k\cdot\mu_{kj}\cdot\omega_{kj} \\ H_s^{kj} &= \sum_\lambda f_s(\lambda)\cdot\frac{I_s(\lambda,\mu_{kj})}{I_s(\lambda,0)}\cdot a_k\cdot\mu_{kj}\cdot\omega_{kj} \\ H_f^{kj} &= \sum_\lambda f_f(\lambda)\cdot c_f(\mu_{kj})\cdot a_k\cdot\mu_{kj}\cdot\omega_{kj}.\end{aligned} \tag{22}$$

The first term in Eq. 21 provides the contribution of spots, while the second is the contribution for the regions with faculae.

The effect of a transiting planet is modelled as a circular dark spot. Therefore, the variations produced on the global CCF can be computed by

$$\Delta C_j^{tr}(v) = -\sum_k C_p(v_k)\cdot H_p^{kj}\cdot p_{tr}^{kj}, \tag{23}$$

As in Eqs. 14, 16 and 17, if the planet occults part of an active region, the corresponding fraction of the surface is computed within p_{tr}^{kj} instead of the occulted p_s^{kj} or p_f^{kj}.

Finally, the total CCF simulated for the observation j is obtained by adding the contribution of the active regions (Eq. 21) and the transiting planet (Eq. 23) to the signature of the unspotted photosphere (Eq. 18):

$$C_j(v) = C^{im}(v) + \Delta C_j^{ar}(v) + \Delta C_j^{tr}(v). \tag{24}$$

The function $C_j(v)$ is fitted with a Gaussian profile using a least square algorithm to obtain an accurate measurement of the peak, which is associated to the RV measurement for the time step j of the simulation. The fit is made for the data contained in a window of width $\Delta v_{\rm CCF}$, specified in the input parameters, around the maximum of $C_j(v)$. A value of 20 to 40 km s^{-1} for $\Delta v_{\rm CCF}$ has been tested to be optimal for the simulations of Sun-like stars. This needs to be adjusted according to the stellar rotation and radius, ensuring that both wings and parts of the continuum are inside the window of the CCF. The FWHM of the Gaussian fit is also provided as an output of the simulations, as this is related to broadening mechanisms (Gray 1992). Finally, the bisector span is computed at each time step of the simulation from the difference between the mean of the 60 to 90% interval of the bisector of the CCF in Eq. 24 and the 10 to 40% interval. This definition accounts for the inverse slope of the bisector (BIS), as introduced by Queloz et al. (2001), and it is the most commonly used in recent studies based on HARPS data (Baştürk et al. 2011; Figueira et al. 2013).

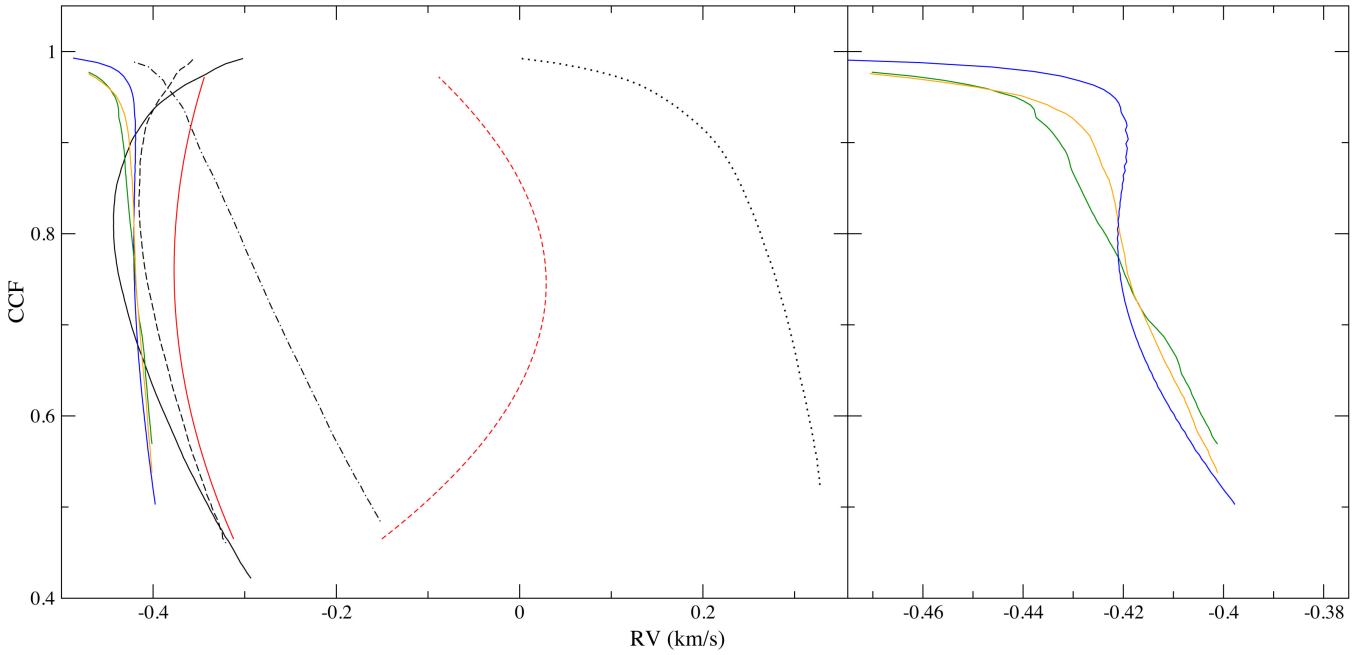

Fig. 6. Left panel: Line bisectors computed using the full HARPS instrument range (~380 - 670 nm) from CIFIST 3D model spectra at μ = 1.0 (black solid line), μ = 0.79 (black dashed line), μ = 0.41 (black dot-dashed line) and μ = 0.09 (black dotted line). Also shown are line bisectors for the solar observed spectra for a quiet Sun region (red solid line) and a spot (red dashed line), and the the bisector computed with `StarSim` from the integrated CCF of an unspotted photosphere of a Sun-like star (blue solid line). Right panel: Zoom of the left part of the left plot showing a comparison with the bisectors of the Sun-like stars α Cen A (green solid line) and 18 Sco (orange solid line) observed with the HARPS South instrument (X. Dumusque, private communication).

Figure 5 shows the spectroscopic measurements simulated for a single active region on a Sun-like (left) and a K0 star (right), including a comparison with simulations obtained with SOAP 2.0 for the same configurations. Inspection of the RV panel (third from the top) shows that the introduction of faculae (Q = 3) notably increases the influence of stellar surface with inhibited convective blueshift, thus producing a symmetric signal. The ~350 m s^{-1} mean difference between the quiet Sun and sunspot bisectors is the main parameter producing the RV variations. The effects of observed solar bisectors to account for the redshift in the active region introduce asymmetries in the FWHM and the BIS signatures. While being of the same order, the differences with the SOAP 2.0 simulations in these measurements can be explained by a different approach when modelling the center-to-limb variations of the bisectors, both for the quiet photosphere and for the active regions. While SOAP 2.0 uses the same CCF models across the full disk, in `StarSim` we use a more sophisticated and accurate approach of modelling the shape of the bisector by interpolating CIFIST 3D models of different μ angles (see Fig. 6). Also the ~350 m s^{-1} redshift of active regions is scaled with μ, accounting for the projection of the convective motion. As discussed in Appendix B of Dumusque et al. (2014), where a simple limb-shift model of spectral lines is implemented, the approach of SOAP 2.0 can produce spurious phase shifts in the spectroscopic measurements.

Figure 7 shows the radial velocity signature of a single active region on a Sun-like star. The effects of rotation (flux) and convection are displayed separately, both for the case of a spot without faculae (Q = 0) and with surrounding faculae (Q = 3.0). Notice that the flux effect dominates the total RV signal for spots, while active regions with faculae produce a convection dominated signature. While convection is blocked both for spots and faculae, the temperature contrast is much larger in the first, so that the effect of rotation is more important. Those explanations and results can be generalized to rapid rotators as shown by Dumusque et al. (2014).

The `StarSim` tool also computes the level of Ca II H&K chromospheric emission by means of the S index (Wilson 1978; Vaughan et al. 1978; Duncan et al. 1984). The total emission of the visible surface of the star is computed from the contribution of all the surface elements, again accounting for the surface, projection and limb darkening factors of each element (see Eq. 22). As before, to improve efficiency we first integrate the emission of a quiet star and then add the contribution from the active regions and, if necessary, subtract the area occulted by transiting planets (similarly to Eqs. 18, 21, 23, and 24 for the CCF). The S emission from the active regions, as well as from the quiet photosphere elements, were estimated from the measurements reported by Baliunas et al. (1995) and Hall et al. (2007) for the quiet Sun (S_{quiet} ~ 0.164), and for the active Sun (S_{act} ~ 0.2), assuming a ~ 0.3% spot coverage and Q = 0 and Q = 3 (Balmaceda et al. 2009; Foukal 1998; Chapman et al. 2011). Simulated time series data of the S index for a Sun-like star with a single spot are displayed in the bottom panel of Fig. 5. Considering the previous assumptions, the variability is in agreement with the measurements by Baliunas et al. (1995) comprising several complete solar cycles.

3. Simulated spectral signature of active regions

As presented in Sect. 2, `StarSim` allows to model the photometric and spectroscopic variability of an active star with cool starspots and hot faculae modulated by stellar rotation. The spectral signature of active regions is defined as the dependence of

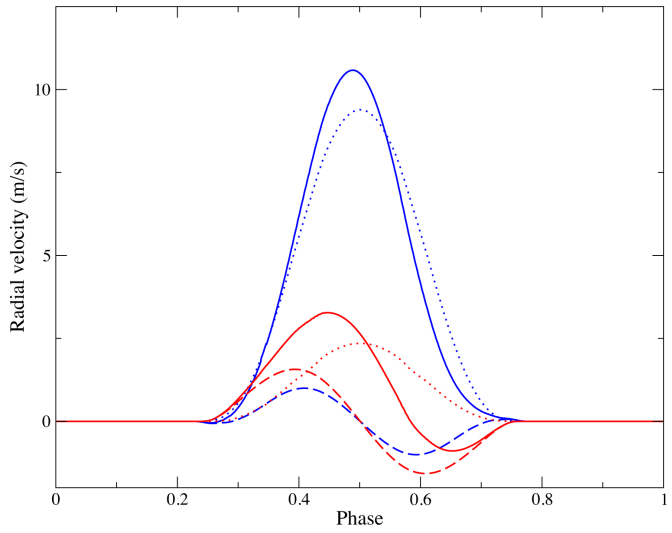

Fig. 7. RV shifts produced by a single spot at $\theta = 90°$ with a size of $A_{\rm Sn} = 1.6 \cdot 10^{-3}$ stellar surfaces on a Sun-like star with $i_* = 90°$, both for a simulation without ($Q = 0$, in red) and with faculae ($Q = 3.0$, in blue). The result of simulating a rotating star ($P_{\rm rot} = 25$ days) with no convection is plotted with a dashed line, showing the flux effect. The simulation of a convective star with no Doppler shifts is plotted with a dotted line. Both effects are included in the results plotted with a solid line. The HARPS passband is used to compute all the RVs.

the flux variability or photometric jitter introduced by active regions with the equivalent wavelength of the observations. This can only be measured from time series spectroscopy or multi-band photometry of spotted stars and provides the key for the estimation of spots temperatures and sizes, which remain degenerated when observations in a single photometric band are available. Pont et al. (2013) provide measurements of the temperature contrast of spots in HD 189733 (see also Pont et al. 2008; Sing et al. 2011) by computing the wavelength dependence of the amplitude of the flux increase caused by a spot occultation observed during a planetary transit, yielding $\Delta T_{\rm spot} \geq 750$ K, which is consistent with a the mean projected filling factor of 1 - 3% computed from the variability in the MOST photometry (Croll et al. 2007; Miller-Ricci et al. 2008; Boisse et al. 2009).

The methodology implemented in `StarSim` allows to model the spectral signature of spots and faculae from multi-band observations of activity effects. We may adopt the flux rms as an adequate measurement of the variability in a given light curve. Simulations for a test case Sun-like star ($T_{\rm eff} = 5777$ K, $\log g = 4.5$ and solar abundances) with a rotation period of 25 days are performed in order to generate time series photometry for 12 different filters, ranging from the visible to the mid-IR (Johnson UBVRI, 2MASS JHK and Spitzer IRAC bands). The time series photometry covers 75 days with a cadence of 1 day. The stellar surface is populated with a distribution of 3 to 8 active regions composed of spots of an average size $\bar{A}_{Sn} = 2 \cdot 10^{-3}$, in units of the total stellar surface. Two different scenarios are considered regarding the presence of faculae, assuming $Q = 0.0$ and $Q = 5.0$. The temperature contrasts are initially set to $\Delta T_{\rm spot} = 350$ K and $\Delta T_{\rm fac} = 30$ K. The active regions are located at a mean latitude of ±40° and evolve with a typical lifetime of 40 days.

The resulting photometric signature for each configuration is computed in the Johnson UBVRI, 2MASS JHK and Spitzer IRAC filter passbands, thus providing the spectral signatures of the active regions computed from ∼ 300 to ∼ 8000 nm. These are presented in Fig. 8, together with a snapshot of the stellar surface map at the initial time of the simulations without faculae. The same active region map is used for all the simulations. In a first step, a scenario with $Q = 0.0$ was considered and $\Delta T_{\rm spot} = 350$ K and $\bar{A}_{Sn} = 2{\cdot}10^{-3}$ were assumed. The resulting spectral signature is plotted with a black line in the middle panel of Fig. 8. Then, we scaled the spot areas to ±50% and we searched for the $\Delta T_{\rm spot}$ values that preserve the flux rms in the Johnson V band. We obtained $\Delta T_{\rm spot}^{+50\%} = 230$ K and $\Delta T_{\rm spot}^{-50\%} = 730$ K for the enlarged and reduced spots, respectively. The resulting spectral signatures for these two configurations of temperature contrasts and sizes of spots are also plotted in the middle panel of Fig. 8 with a red line and a blue line, respectively. Whereas the variability differs more than $2{\cdot}10^{-3}$ (relative flux units) in the ultraviolet, the signature of the spots is barely distinguishable for the three parameter configurations in the rest of the spectral range. The results change significantly when faculae are included around the spots, as shown in the bottom panel of Fig. 8. We assume $Q = 5.0$, which is slightly lower than the mean solar value (Chapman 1987; Lanza et al. 2003), and $\Delta T_{\rm fac} = 30$ K in all cases. Then, we recompute the spectral signature for the same three configurations previously described. In this case, the spot temperature contrasts that preserve the photometric variability in the Johnson V band are $\Delta T_{\rm spot}^{+50\%} = 275$ K and $\Delta T_{\rm spot}^{-50\%} = 550$ K. The signature of active regions is dominated by the emission of bright faculae in the near and mid infrared, especially for the configurations with the lowest spot temperature contrasts, $\Delta T_{\rm spot} = 350$ K (black line) and $\Delta T_{\rm spot} = 275$ K (red line), as we see an increase in the rms after ∼ 1500 nm.

These results show that the determination of the basic spot parameters require spectrophotometric time series measurements at the 10^{-4} precision level. On the other hand, the presence and amount of faculae can be more easily measured in the red and near-IR bands, since there the photometric signature of the simulated configurations differ by ∼ 10^{-3}.

4. Modelling real data

4.1. Algorithm description

`StarSim` is intended to generate simulated signals from arbitrary distributions of stellar and activity parameters, as described in Sects. 2.2.2 and 2.2.3, with a better precision than other existing tools. The problem we are facing here is so called inverse problem, consisting in finding the causal factors of an observation. In this case, the aim is obtaining a dynamical spot configuration that fulfills the photometry time series. In the case of active stars, this could be a clue step for disentangling planetary signals, specially those existing in RV data. The methodology used in `StarSim` to simulate the stellar surface is also implemented to perform the inverse problem and obtain detailed stellar surface maps that best fit the observed photometric signature produced by $n-$ active regions. The observables are described as

$$y_i(t_i) \simeq f_i(s_j, a_k) \qquad (k = 1, \ldots, n), \tag{25}$$

where y_i is the measurement at time t_i, f_i is the model, a_k are the stellar parameters, and s_j is the configuration of active regions. The generation of the functions f_i is described in Sect. 2.2.2 and Sect. 2.2.3 for the photometric and the spectroscopic observables, respectively.

In our case, `StarSim` performs a Monte Carlo Simulated Annealing minimization (MC-SA). This is a generic probabilistic

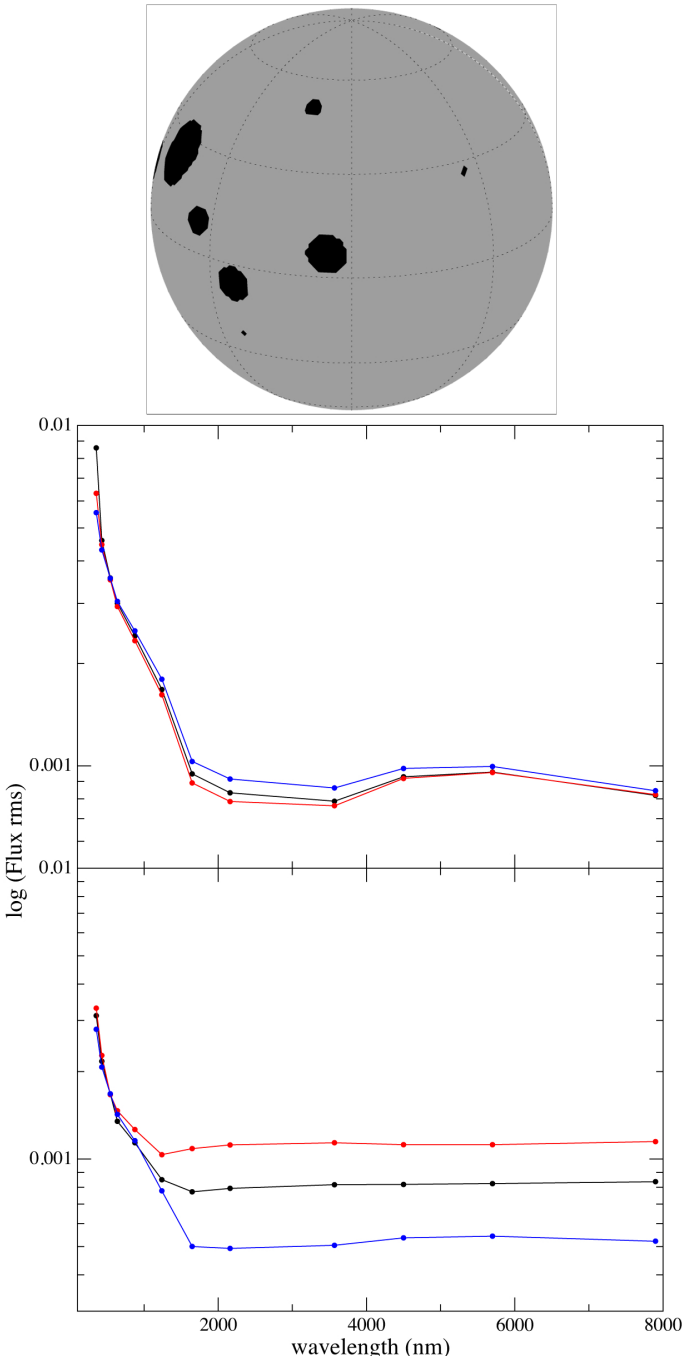

Fig. 8. Top panel: map of the initial distribution of active regions as used for the simulations in Sect. 3 in the case of $Q = 0.0$. Middle panel: the spectral signature (flux rms vs. wavelength) for three different configurations of active regions normalized to the same resulting rms in the Johnson V band: $\Delta T_{\rm spot} = 310$ K and $\bar{A}_{Sn} = 2 \cdot 10^{-3}$ (black line), $\Delta T_{\rm spot}^{+50\%} = 230$ K and a 50% increase in the area of the spots (red line), and $\Delta T_{\rm spot}^{-50\%} = 730$ K and a 50% decrease in the area of the spots (blue line). Bottom panel: same as the middle panel including facula regions with $Q = 5.0$ and $\Delta T_{\rm fac} = 30$ K, where the red line corresponds to $\Delta T_{\rm spot}^{+50\%} = 230$ K and the blue line to $\Delta T_{\rm spot}^{-50\%} = 550$ K.

global optimizer that allows to find a reasonably good approximation to the optimum in large configuration-space problems. Although this method has been used mainly in discrete spaces, it is also appropriate to tackle continous problems as the case of continous parameters of the spot list. One of the significant advantages of this optimization technique is the proven robustness against local minima in noisy surfaces (Kirkpatrick et al. 1983), which makes it an interesting approach to optimize models involving a *large* number of parameters. The name of the algorithm –and its associated nomenclature– comes from the term "annealing" in metallurgy, a technique involving a scheduled cooling of metals to modify the size of crystals and reduce their defects.

The aim of the fitting process is to find a map of active regions that minimizes the χ^2,

$$\mathcal{S}^* = \arg\min_{s_j \in \mathcal{S}} \chi^2(\text{data}\,;\, s_j), \tag{26}$$

where χ^2 is evaluated between the model and the data,

$$\chi^2 = \sum_{i=1}^{N} \frac{[y_i - f_i]^2}{\sigma_i^2} \tag{27}$$

and σ_i are the errors associated to de data.

The activity map s_j is defined as a set of parameters containing the coordinates, initial time, lifetime and size of a preselected number of active regions, n.

$\mathcal{S}_j = \{\ t_{init},\ t_{life},\ \phi$ (colatitude), λ (longitude), radii $\},\ j = 1, \ldots, n$

where s_j is a specific configuration of active regions from all the possible sets, $\mathcal{S}$, and $\mathcal{S}^*$ is the optimal configuration.

Further details on the MC-SA procedure are given in Appendix A together with the parameters as used in `StarSim`.

4.2. Current status of StarSim

The `StarSim` tool is currently capable to generate simulated photometric and spectroscopic signals as described in Sections 2.2.2 and 2.2.3. The `StarSim` code is currently written using a combination of Fortran and C routines. The simulations ran on an Intel Core i7-3770 CPU at 3.40 GHz produced a time series of 1000 phases in 60 seconds for photometric data (see Sect. 2.2.2) of a Sun-like star in the Johnson V band for a random distribution of four spots. In the case of high-resolution spectroscopic data (see Sect. 2.2.3), the same simulation takes 210 seconds.

The algorithm to perform the inverse problem by means of a simulated annealing procedure (see Sect. A) is currently implemented only in the case of a single photometric time series. The inclusion of RV data, as well as multiple photometric passbands, would require a more sophisticated treatment of errors and is being under consideration for a new version of the tool. At the moment, simultaneous series data for active stars are being studied with `StarSim` by simulating a grid of RV solutions from the best fit of the photometry. An example including a discussion on the constrains provided by the analysis on the stellar and activity parameters is presented for the case of HD 189733 in next section.

5. A case example: HD 189733

5.1. System parameters

The exoplanet host HD 189733 is a bright ($V = 7.67$ mag) K0V-type star known to present significant rotation modulation in its light curve (Winn et al. 2007) with a period of ~ 11.9 days and to be relatively active from the measurement of the chromospheric

Table 2. Parameters for the system HD 189733

Parameter	Value	Reference
$T_{\rm eff}$	5050±50 K	M06
$\log g$	4.53±0.14	M06
[Fe/H]	-0.03±0.04	M06
$\Delta T_{\rm spot}$	∼560 K	L11
Q	0.0	L11
P_0	11.953±0.009 days	H08
i_*	85.5° ± 0.1°	T09
$A_{\rm Sn}$	$5 \cdot 10^{-4} - 3 \cdot 10^{-3}$	L11
$P_{\rm planet}$	2.2185733±0.0000014 days	MR08
$R_{\rm planet}/R_*$	0.1572±0.0004	P07
b	0.671±0.008	P07
γ	1.4±1.1°	W06

References: M06 (Melo et al. 2006); MR08 (Miller-Ricci et al. 2008); P07 (Pont et al. 2007); L11 (Lanza et al. 2011a); H08 (Henry & Winn 2008); T09 (Triaud et al. 2009); W06 (Winn et al. 2006).

activity indices (Wright et al. 2004; Moutou et al. 2007). The existence of a hot Jupiter planet with a short period (2.2 days) was first announced by Bouchy et al. (2005). Several studies have reported the presence of activity effects on the RV measurements of up to ∼ 15 m s^{-1} (Lanza et al. 2011a; Bouchy et al. 2005) and have obtained information about the stellar surface photosphere from the modelling of the flux variations (Croll et al. 2007; Lanza et al. 2011a). The parameters for the HD 189733 system, as used in all the simulations in this section, are presented in Table 2.

Miller-Ricci et al. (2008) studied the transit timing variations (thereafter TTVs) and the transit depth variations (thereafter TDVs) from 6 transit observations obtained by MOST, which monitored HD 189733 for 21 days during July - August 2006. No significant effects of spot crossing events were observed at any phase of the transits, but no further discussion on the possible effects of non-occulted spots was presented. When a transiting planet passes in front of a starspot, the depth of the transit is shallower in a portion of the transit due to the fact that the planet has crossed a dimmer region of the photosphere. In the case of low signal-to-noise observations that cannot resolve the event, this would affect the overall transit depth fit. Also, TTVs of ∼ 1 minute would be induced if a spot crossing event occurred at the ingress or egress phases of the transit. See Barros et al. (2013) for an extensive discussion. On the other hand, non-occulted spots present during the transit time introduce variations of the stellar flux with chromatic dependence. Thereafter, they can produce a bias in the transit depth measurement and modify the signature of the atmosphere of the planet as studied by transmission spectroscopy. Since a spot is modelled as a cooler region on the stellar surface, its signal will be stronger in the blue, where the flux contrast increases, than in the red.

Pont et al. (2007) described some properties of the starspot groups in HD 189733 from the observation of two spot crossing events. The features observed in the transit light curves show a wavelength dependence and can be explained by the presence of cool regions with $\Delta T_{\rm spot}$ ∼1000 K and a size of ∼ 12000 km to ∼ 80000 km, which correspond to $A_{\rm Sn}$ of $\sim 2 \cdot 10^{-5}$ to $\sim 6 \cdot 10^{-3}$ in units of the total stellar surface.

Lanza et al. (2011a) obtained a more detailed map of the active region distribution by modelling MOST photometry covering 30.5 days from July 17 to August 17, 2007, and RV measurements from SOPHIE obtained for the same time span (Boisse et al. 2009). Their approach was based on reconstructing a maximum entropy map with regularization. This allows to model the longitudinal evolution of active regions over time, but the information on the latitudes is lost particularly when the inclination of the stellar rotation axis is close to 90°, as it is the case for HD 189733. So the method tends to assume that the spots are located near the stellar equator, hence adopting the minimum possible size for the spots to simulate the observed variations. The results of Lanza et al. (2011a) show that the data can be explained by the presence of 2 to 4 active regions yielding a photometric fit with an rms of $4.86 \cdot 10^{-4}$ in relative flux units and a resulting RV curve that in rough agreement with the observed data (to within a few m s^{-1}). The individual spots cover 0.2 to 0.5% of the stellar disc and their lifetimes are comparable or longer than the duration of the MOST observations (i.e., ∼ 30 days), while the rise and decay occur in 2-5 days. In this case, the spot contrast is computed assuming a spot effective temperature of 4490 K (i.e., $\Delta T_{\rm spot}$ = 560 K). A different spot contrast would imply a change in the absolute spot coverage to explain the same photometric signature (Pont et al. 2007), but it would not have a significant effect in a single band photometric time series. Fares et al. (2010) measured the equatorial and polar rotation periods obtaining 11.94 ± 0.16 days and 16.53 ± 2.43 days, respectively, thus giving a relative amplitude of $\Delta\Omega/\Omega = 0.39 \pm 0.18$, which is very similar to the Sun (so we assume $k_{\rm rot} = 1$). Then, the migration rates of spots measured by Lanza et al. (2011a) indicate that most of the spots are located at latitudes ranging from 40° to 80°.

5.2. Activity model

We analyze the MOST photometry dataset from 2007 (Lanza et al. 2011a). After removing the transits, the series contains 414 measurements with a mean error of 1.15×10^{-5} in relative flux units. The RV data from the SOPHIE spectrograph were obtained from July 13 to August 23, 2007, providing a data set of 33 RV measurements. The combination of these simultaneous data sets represents a great opportunity to test the methodology of `StarSim` to obtain a surface model of activity for HD 189733.

The `StarSim` program with the minimization methodology presented in Sect. 4.1 was used in order to obtain a surface map for HD 189733. In a first approach, the MOST photometric dataset was modeled, no faculae were considered (see Lanza et al. 2011a), and the spot sizes were assumed to evolve with the mean solar growth/decay rate (i.e. $a_{\rm rd} \simeq 1°$, Martinez Pillet et al. 1993; Petrovay et al. 1999). A map of 90 active regions with a grid resolution of $1° \times 1°$ was fitted for their position, time of appearance and lifetime, while the stellar parameters were fixed to the ones specified in Table 2. Despite considering a relatively high number of active regions, the minimization algorithm tends to concentrate the spots in groups, as expected. The number was adjusted to reduce the rms of the fit while preventing isolated small spots to appear in the modelled surface. Three maps containing 90 spots were randomly generated and used as initial conditions for three different fitting runs and the simulated annealing procedure was permormed as described in Sect. A in order to determine the convergence. The final rms of the residuals is $3.8 \cdot 10^{-4}$ in relative flux units for all the solutions, which only present visible differences for the latitudes and sizes of some of the spot groups. The light curve model for the first run is shown in Fig. 9.

The photometric fit that we obtain is of better quality than those published to date and our model is able to describe with

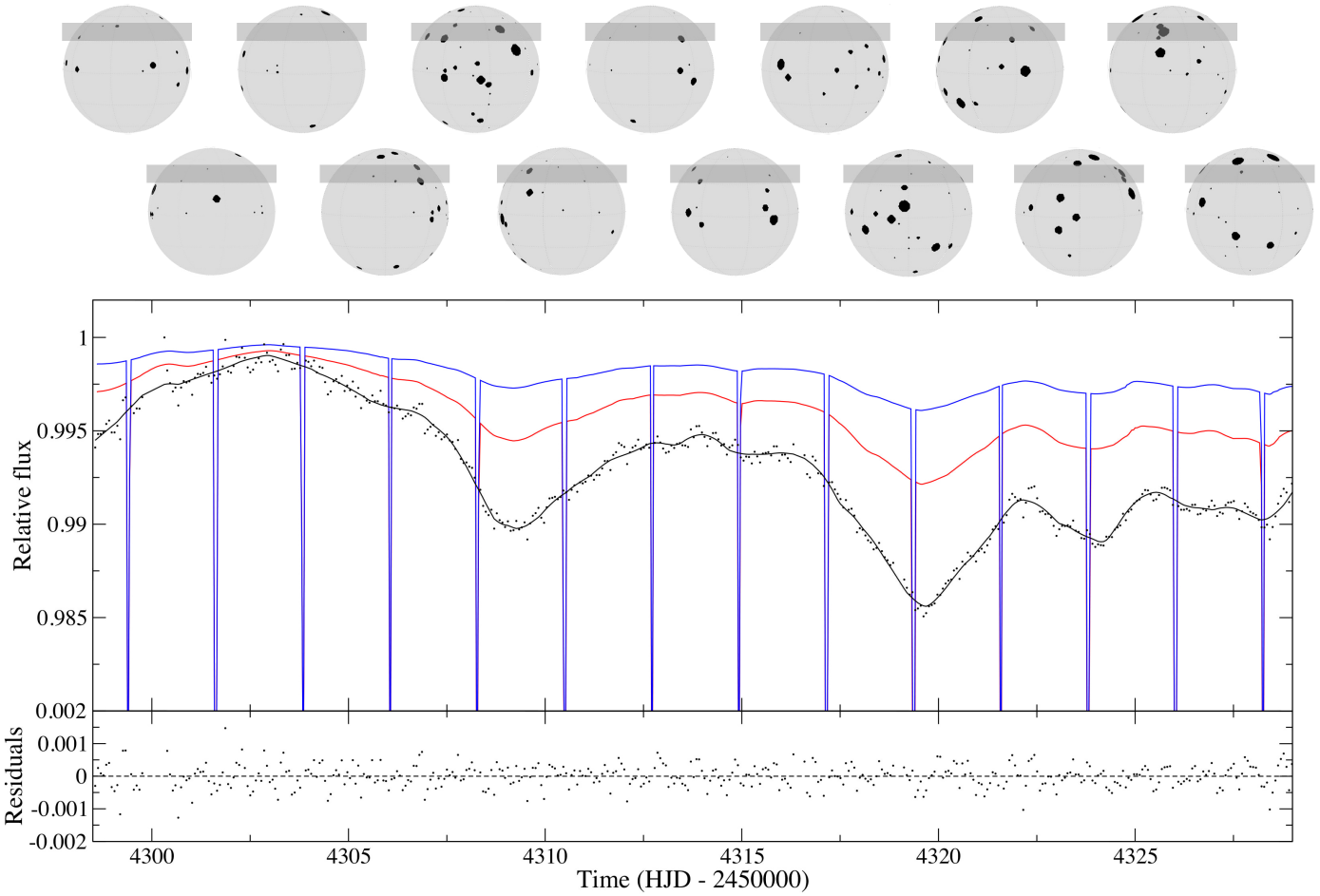

Fig. 9. Synthetic light curves generated for HD 189733 with the methodology described in Sect. 2.2.2, assuming the parameters described in Sect. 5.1 and the modelled activity map, for the MOST (black line), 2 MASS J (red line) and IRAC 2 (blue line) passbands. The flux is in relative units with respect to the maximum along the light curve and shows the 14 analysed transit events. Observed data from MOST is plotted with black dots. The projected maps of the stellar surface at the mid-transit times are plotted in the upper part, including a dark grey band that indicates the region of the star occulted by the planet.

precision many of the features of the photometry. The distribution of active regions derived from the photometric fit and the parameters defined in Table 2 were adopted in order to synthesize the RV curve for the same time span and for the instrumental passband of SOPHIE. The result is plotted in Fig. 10 together with the SOPHIE data. The model and the observed RV variations are generally in good agreement except for the regions around ~HJD 2454309 and ~HJD 2454327, where probably a higher evolution rate for the spots is needed in order to reproduce the rapid modulations. However, we could not reproduce them when exploring different initial parameters for the active regions, so they are either caused by instrumental effects, or such variations are not explained by spots and faculae. The analyses presented by Lanza et al. (2011a) and Aigrain et al. (2012) using photometric spot models were also unable to reproduce the rapid RV variations. When excluding the three measurements between HJD 2454307 and 2454310, the rms of the residuals of our model is 5.45 m s^{-1}, which improves the results from the previous studies (5.55 m s^{-1} from Lanza et al. 2011a and 6.6 m s^{-1} from Aigrain et al. 2012) and is close to the typical instrumental uncertainties of SOPHIE (~5 m s^{-1}).

A further step forward in the analysis would be to include the SOPHIE RVs in the inverse problem and to perform a simultaneous fit. However, several tests indicated that the number of data points and the precision of the velocity data are too low for the fitting algorithm to work properly. Alternatively, we used the RVs to investigate the effect of several parameters that are usually adopted *ad hoc* or from independent criteria because of the lack of sensitivity of the light curve. The parameters are the zero point of the photometric flux (i.e., immaculate flux level), the stellar equatorial rotation period ($P_{\rm rot}$), the facula-to-spot area ratio (Q) and the temperature contrast of the active regions.

The StarSim code was used to fit the photometry with the same assumptions as described before and by exploring a grid of possible values for the four parameters in sequential and independent fashion. In this case, a model of 30 active regions was used for simplicity. The results are shown in Fig. 11. The panels on the left show the rms of the photometric fit as a function of the parameter value, while the panels on the right display the simulated RV curves compared with the observed data. As expected, all investigated parameters have very little influence on the quality of the photometric fit except for the spot temperature contrast, which shows a broad, flat minimum around $\Delta T_{\rm spots} \sim 600$ K, in agreement with Lanza et al. (2011a). Regarding the impact on the RVs, it is observed that the variations in the photometric zero point and the rotational period of the star

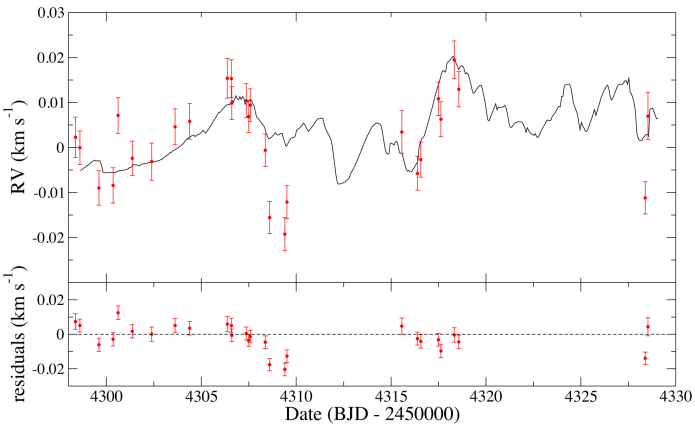

Fig. 10. Upper panel: RV model curve generated with `StarSim` for HD 189733 (black solid line) compared to the SOPHIE data (red dots). Bottom panel: residuals between the data and the model.

induce phase differences in the simulated RV curves. Figure 11 also shows that the value of Q has a very strong influence on the RV amplitude. The photometric fit, although not very significantly, favours values of Q close to 0, and this is also in agreement with the modest observed RV variation. The amplitude of the RV signal is also sensitive to the spot temperature contrast. The results of the simulations shown in the right panel d) indicate that $\Delta T_{\rm spots} \sim 400 - 500$ K are in close agreement with the SOPHIE data, while higher values show increasing deviations.

We see notable differences in the RV simulations adopting different parameters, thus indicating that the degeneracies present could be partially broken if RV data are considered in the inverse problem. Note that the initial conditions of the distribution of active regions (positions and sizes) are randombly chosen and could also have an impact on the simulated RV curves shown in the right panels of Fig. 11. This, however, is not a concern when the full inverse problem is considered, since different random realizations can be used to explore the entire parameter space. In this case the modelling would allow for a full description of the stellar surface, including active region parameters, and thus a complete characterization of the stellar activity properties. The application of this procedure to a sample of stars would help to understand some key aspects and therefore provide means to correct RV measurements from the unwanted effects of stellar activity in a self-consistent way.

5.3. Activity effects in transit photometry

Synthetic light curves for HD 189733 including planetary transits were generated using the methodology presented in Sect. 2.2.2 for the 12 filters used in Sect. 3 for the same time span as the MOST photometric data modelled in Sect. 5.2. This covers three complete rotation periods of the star (i.e., 14 transits of the exoplanet HD 189733b). The surface map from the photometric model obtained in Sect. 5.2, consisting of 90 spots, was considered for all the simulations. The resulting light curve has a maximum amplitude of $\sim$ 0.012 mag in the Johnson V filter. The light curves for the 2 MASS J and the IRAC 2 passbands are plotted in Fig. 9.

For each passband, data segments of $2 \cdot T_{14}$ (i.e., twice the total duration of the transit) around the transit mid point were selected for analysis. The out-of-transit baselines at either side of the transit were used to fit a parabolic trend that was subsequently subtracted from the in-transit observations. The data points affected by spot crossing events were removed and not considered for analysis. Then, a Nelson & Davis (1972) model as implemented by Popper & Etzel (1981) was fitted to each individual transit using the JKTEBOP code (Southworth et al. 2004) to measure the transit depth and the mid transit time. In a first step, precise quadratic limb darkening coefficients were obtained for each passband by fitting a model to a transit light curve generated for an immaculate photosphere. With these limb darkening coefficients, the full series of transits was analysed by fitting the planet radius and the zero point of the ephemeris. The rest of the parameters were fixed to the ones shown in Table 2.

A number of spot crossing events have been detected in HD 189733b transit observations (Miller-Ricci et al. 2008; Sing et al. 2011; Pont et al. 2013). The observed occurrence of these events combined with the assumption that the planet is crossing a typical zone of the stellar surface in terms of spot coverage, leads to an estimate of $1-2\%$ of projected spot filling factor (Sing et al. 2011), which is in agreement with the results by Lanza et al. (2011a) and the spot maps used in this work. In the case of our synthetic data, as the active region map is poorly constrained due to the low signal-to-noise ratio of the MOST observations (see Lanza et al. 2011a), and especially the latitudes of the spots are degenerated, we do not expect all the events from the MOST data to be accurately reproduced by the model. For this reason, the data affected by spot crossing events were removed before fitting the transit models in order to study and quantify the chromatic effects of non-occulted spots.

The results of the analysis of synthetic transit data are displayed in Fig.12, showing the chromatic dependence of the planet radius determination for each transit event. All transits present some level of influence from non-occulted spots. The measurements for R_p/R_* are normalized at the values obtained for the transit light curve simulated on an unperturbed photosphere.

As the presence of spots in the stellar surface changes the overall transit depth measurement (i.e. the duration of the transit is much shorter than the typical changes in the projected filling factor), there are no significant differences on the measured times of mid-transit. Spots not occulted by the planet introduce a monotonic regular behavior from the UV to mid-infrared wavelengths. Therefore, the spectral signature of the spots clearly dominates the effects introduced on the transit depth, as seen in Fig. 12. The results for the transit depth measurements are also displayed vs. the projected filling factor of spots (measured at the mid-transit times) in Fig. 13 for the 12 analysed filter passbands. The dispersion in this plot is due to the gaps introduced in the data when removing spot crossing events. For all transit simulations, the effect produced by spots is much stronger in the blue than in the mid-infrared, as a consequence of the spectral signature of the spots. The shift on the transit depth measurement introduced by non-occulted spots is scaled with the instantaneous filling factor, ranging from $\Delta\left(R_p/R_*\right) \sim 0.0001$ for a nearly unspotted surface (3rd transit, at HJD$\sim$2454301.8 in Fig. 9) to ~ 0.001 for a projected filling factor of $\sim 3\%$ (10th transit, near HJD$\sim$2454319.0). This is an important information to take into account when correcting the transit depths for activity, as observations of HD 189733 show that there is significant variability in the filling factor over time. Note that in order to obtain the spot filling factors affecting our simulations (shown in Fig. 13) we assumed that the maximum of the MOST photometry as the unit of measure for the flux in order to normalize the light curve

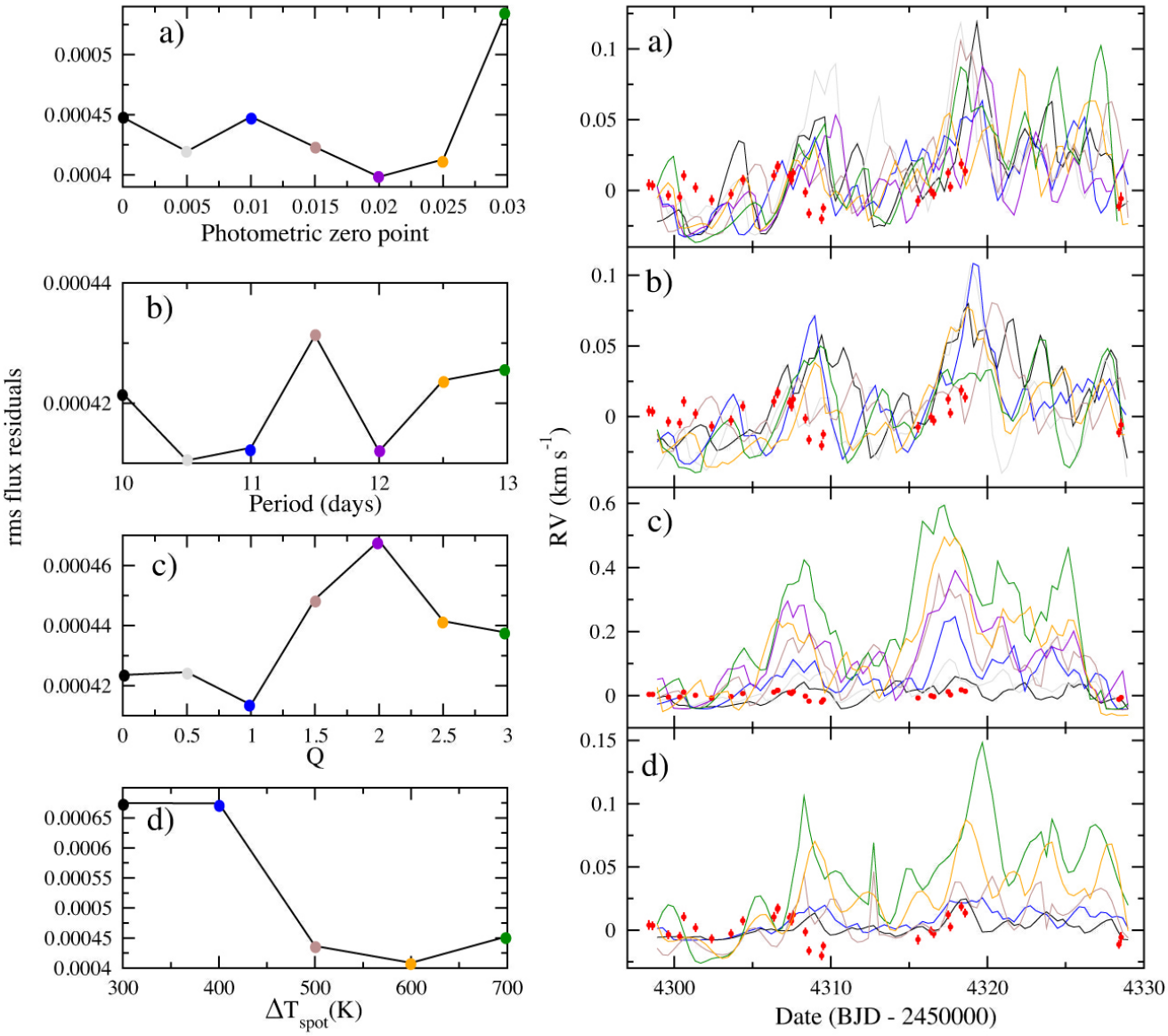

Fig. 11. Left panels: rms of the residuals from the fit to the MOST light curve with a model of 30 active regions vs. four stellar parameters. Right panels: simulated RV curves resulting from the models compared to the SOPHIE data (red dots). The four pairs of panels show the dependence of the rms of the light curve fits and the RV signature on a) the zero point of the photometry, b) the stellar rotation period, $P_{\rm rot}$, c) the facula-to-spot area ratio, Q, and d) the temperature contrast of the spots, $\Delta T_{\rm spot}$. The colour code of the lines in the right panels correspond to the dots in the left panels.

(Lanza et al. 2011a). Although the evolution of the spot map we used accurately reproduces the variations, a zero point in the filling factor of spots could be present. This is not still clear from the results shown in Fig. 11, as discussed in Sect. 5.2. However, the statistics of spot crossing events during HST observations and the characteristics of the transmission spectrum in the visible (Sing et al. 2011), indicate that the projected spots filling factor is not much higher than 1-2 %.

6. Discussion and conclusions

We present a methodology, in the form of the `StarSim` tool, to simulate the photosphere of rotating spotted stars. This allows us to generate synthetic photometric and spectroscopic time series data from a set of given parameters and a library of stellar atmosphere models. The main purposes of this methodology are the characterization of the effects produced by activity in time series observations, especially multi-band studies of exoplanetary transits, and the design of strategies for the minimization of activity effects, both when searching and characterizing exoplanets. Several aspects should be taken into account to discuss the reliability of the results and their interpretation.

First, we assumed LTE stellar models for the emission of the quiet photosphere and also for the spot and facula regions. This is a limitation imposed by the availability of stellar model libraries with high resolution spectra. The synthetic spectrum shown in Fig. 2 correctly fits the observed spectrum of a spot and provides a temperature contrast in agreement with most of

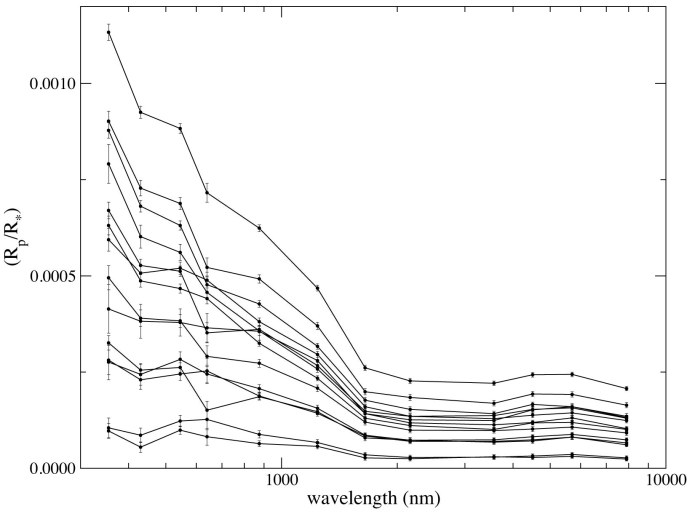

Fig. 12. Variations on the transit depth R_p/R_* vs. the central wavelength of 12 different filters produced by several configurations of spots on the 14 synthetic transits of HD 189733b in the simulated light curves, relative to the transit depth in an unperturbed transit. Data affected by spot crossing events have been removed.

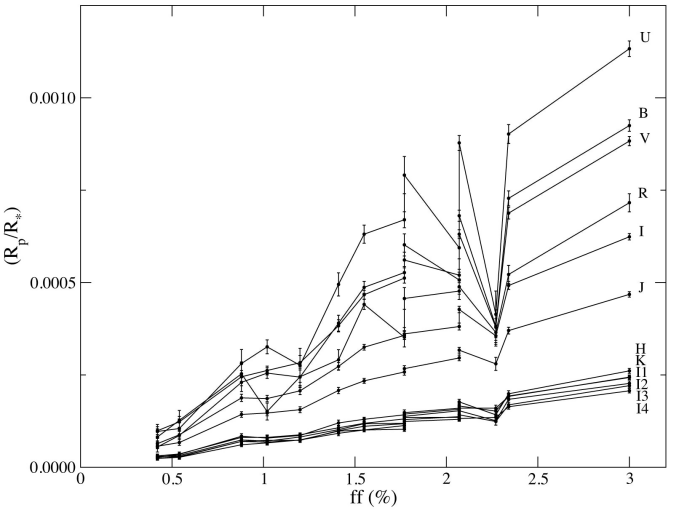

Fig. 13. Variations on the transit depth R_p/R_* vs. the projected filling factor of spots at the mid transit times for the 12 simulated passbands.

the values in literature (see Sect 2.1). However, certain lines are not well reproduced, which suggests that the spot spectrum is different from a cooler stellar photosphere. In the case of faculae, no high resolution observed spectra are currently available, and the most recent NLTE models for the Sun are the ones presented by Fontenla et al. (2009). The differences in the spectrum of active regions mainly affect the existence of certain lines, but have no significant impact on the flux when considering a broad range of the spectrum. Therefore, the currently used models are suitable for the characterization of activity effects in the observations for most of the photometric instrumentation. Some more considerations on the influence of the models for the different photospheric features will be discussed in a future paper addressing strategies for the correction of RV measurements in active stars. Such RV measurements are usually obtained by using the information content of the lines in the whole observed spectral range. On the other hand, optimized measurements can be made by excluding the spectral lines or ranges that are most affected by activity.

Second, given the requirements of this work, the maps of active regions currently used in our simulations are limited to a model of circular spots with a surrounding facula in the shape of a corona, instead of a more complex structure with groups of small spots. Such simple configurations of active regions have proven to adequately reproduce photometric and spectroscopic signature in active stars (Eker 1994; Lanza et al. 2003; Dumusque et al. 2014; Dumusque 2014). However, `StarSim` also allows modelling spots of any shape by including an unlimited number of spots of a small size on the stellar surface. Our approach is very similar to that of Lanza et al. (2003) and subsequent papers that use this type of spot maps to model the surface of active stars. In such case, the regularization of the maximum entropy algorithm provides a smooth distribution of active regions instead of a more irregular surface map populated with a lot of small spots.

Third, several assumptions based on solar data are made in our simulations. This has to be kept in mind when using `StarSim` for stars other than Sun-like. Indeed, the limb brightening law implemented for facula regions is a model based on solar observations. The same applies to the rest of the parameters of faculae, such as the temperature contrast. The evolution rates and lifetimes of active regions have only been measured for a few stars from the various techniques that allow modelling of the stellar surface (Hussain 2002; Strassmeier et al. 1994a,b; Petrovay & van Driel-Gesztelyi 1997; Petrovay et al. 1999). While the previous assumptions affect some parameters that can be adjusted when more information from observations is available, our approach to model activity effects on convection is more intimately linked to solar observations in all cases. The center-to-limb convection profile of the quiet photosphere is implemented from solar CIFIST 3D models. Also, solar high-resolution observations are used to obtain accurate models for the bisector of active regions. Our approach to model convection was tested to perform at the $\sim$1 m s^{-1} precision in some comparisons with Sun-like stars. Finally, the chromospheric emission data produced by our model is based on solar observations of the S index.

An example of the capabilities of the methodology for the characterization of activity effects is presented for the case of a Sun-like star with a typical distribution of active regions. The spectral signature (flux rms vs. wavelength) of the active regions is studied in visible and IR passbands for several configurations of the parameters of the stellar surface. Different configurations of the temperature contrast and the typical area of the spots are found to show a very similar signature when no faculae are introduced. In the presence of faculae (Q = 5.0, $\Delta T_{\rm fac}$ = 30 K), the wavelength dependence is inverted in the red and near-IR wavelengths when the temperature contrast of the spots is $<$ 300 K, thus being the contribution of faculae dominant. In all cases, the dependence is strong in the visible and near-IR, while no signature is observed in the mid-IR. Real observations of the spectral signature for active stars in visible and near-IR filters may provide new estimations of the facula-to-spot area ratio and the parameters of the spots.

The effects of non-occulted spots on multiband observations of planetary transits were studied by considering the case of the active Sun-like star HD 189733 with a transiting hot Jupiter planet. A Monte Carlo Simulated Annealing minimization algorithm was implemented in `StarSim` and stellar surface maps

were obtained by modelling the MOST photometric data for HD 189733. Several stellar parameters which are usually assumed were explored for degeneracies by using simultaneous RV data from SOPHIE. We show that the RV data includes some additional information that can break these degeneracies, especially for the physical parameters of the active regions and the stellar surface map.

Considering the modelled surface map for HD 189733, photometric light curves were synthetised for 14 transits in 12 different passbands from the optical to the mid-IR, covering a variety of spot surface coverages from $\sim$ 0.4% to $\sim$ 3.0%, and the deviations produced on the planet radius measurements were studied. While in the first case the transit depth measurement remains unperturbed up to the 10^{-4} precision in R_p/R_* for any filter passband, a strong effect is introduced when the star is moderately spotted. Moreover, the difference is wavelength dependent, being $\sim 10^{-3}$ in the blue, and only $\sim 5 \cdot 10^{-4}$ in the mid-IR. Therefore, biases of the order of 10^{-3} can be introduced in R_p/R_* measurements for wavelengths in the optical range if a constant spot filling factor is assumed for the non-occulted spot correction (Sing et al. 2011; Pont et al. 2013; McCullough et al. 2014) instead of considering the appropriate instantaneous spot map. Time series photometry simultaneous to the transit observation campaign would be needed to reproduce the evolution of the filling factor of spots and adequately scale the correction for each transit event. In the near future, space telescopes dedicated to exoplanetary sciences will be able to achieve precisions of $\sim 10^{-4}$ on the atmosphere measurements of super-Earths (Tessenyi et al. 2012), so it is essential to adequately model the spectral signature of activity for such types of observations.

We conclude that the approach presented in this paper to generate synthetic time series data accurately accounts for all the physical processes affecting spectroscopic and photometric variations produced by activity, which currently represents the main obstacle for exoplanet characterization and searches. In fact, our approach can help to model and correct for the effects of activity jitter on photometric and RV observations of extrasolar planets, especially if the system parameters are known and the surface map of the stellar host is simultaneously studied. In comparison with already existing tools to model time series data of active stars (Oshagh et al. 2013a; Boisse et al. 2012; Aigrain et al. 2012; Dumusque et al. 2014), `StarSim` accurately accounts for the line bisector distortions caused by convective blueshift and convection inhibition in active regions, based on recent 3D atmosphere models. Most of the cited tools assume a simple Gaussian model for the spectral lines. In the case of `StarSim`, we consider atmosphere models in order to compute the synthetic CCFs and the flux contribution of the visible surface elements of the star. This allows to preserve all the spectral information of the variability produced by activity effects. Also, our simulations allow studying the effects of the amount of faculae as well as of spot temperature contrasts and sizes on multi-band simultaneous photometry. The methodology is currently being implemented to model fit multi-band photometric and spectroscopic RV observations simultaneously, thus obtaining detailed maps for the characterization of stellar photospheres. Several applications of the methodology to real observations and to the design of optimized strategies for the search and characterization of exoplanets will be presented in a series of papers in the near future. `StarSim` will also help to properly account for stellar activity in the detection and characterization of atmospheres in small planets.

Acknowledgements. E. H. and I. R. acknowledge support from the Spanish Ministry of Economy and Competitiveness (MINECO) and the Fondo Europeo de Desarrollo Regional (FEDER) through grants ESP2013-48391-C4-1-R and ESP2014-57495-C2-2-R. C. J. acknowledges the support by the MINECO - FEDER through grants AYA2009-14648-C02-01, AYA2010-12176-E, AYA2012-39551-C02-01 and CONSOLIDER CSD2007-00050. E. H. was supported by a JAE Pre-Doc grant (CSIC).

References

Aigrain, S., Pont, F., & Zucker, S. 2012, MNRAS, 419, 3147
Albregtsen, F. & Maltby, P. 1981, Sol. Phys., 71, 269
Allard, F., Homeier, D., Freytag, B., et al. 2013, Memorie della Societa Astronomica Italiana Supplementi, 24, 128
Baştürk, Ö., Dall, T. H., Collet, R., Lo Curto, G., & Selam, S. O. 2011, A&A, 535, A17
Badalyan, O. G. & Prudkovskii, A. G. 1973, Soviet Ast., 17, 356
Baliunas, S. L., Donahue, R. A., Soon, W. H., et al. 1995, ApJ, 438, 269
Ball, W. T., Unruh, Y. C., Krivova, N. A., Solanki, S., & Harder, J. W. 2011, A&A, 530, A71
Balmaceda, L. A., Solanki, S. K., Krivova, N. A., & Foster, S. 2009, Journal of Geophysical Research (Space Physics), 114, 7104
Barros, S. C. C., Boué, G., Gibson, N. P., et al. 2013, MNRAS, 430, 3032
Beck, J. G. 2000, Sol. Phys., 191, 47
Berdyugina, S. V. 2005, Living Reviews in Solar Physics, 2, 8
Berdyugina, S. V. & Henry, G. W. 2007, ApJ, 659, L157
Berger, T. E., Rouppe van der Voort, L., & Löfdahl, M. 2007, ApJ, 661, 1272
Boisse, I., Bonfils, X., & Santos, N. C. 2012, A&A, 545, A109
Boisse, I., Moutou, C., Vidal-Madjar, A., et al. 2009, A&A, 495, 959
Bouchy, F., Udry, S., Mayor, M., et al. 2005, A&A, 444, L15
Bouvier, J. & Bertout, C. 1989, A&A, 211, 99
Caffau, E., Ludwig, H.-G., Steffen, M., Freytag, B., & Bonifacio, P. 2011, Sol. Phys., 268, 255
Carlsson, M. & Stein, R. F. 1992, ApJ, 397, L59
Chapman, G. A. 1987, ARA&A, 25, 633
Chapman, G. A., Dobias, J. J., & Arias, T. 2011, ApJ, 728, 150
Ciardi, D. R., von Braun, K., Bryden, G., et al. 2011, AJ, 141, 108
Cosentino, R., Lovis, C., Pepe, F., et al. 2012, in Society of Photo-Optical Instrumentation Engineers (SPIE) Conference Series, Vol. 8446, Society of Photo-Optical Instrumentation Engineers (SPIE) Conference Series, 1
Croll, B., Matthews, J. M., Rowe, J. F., et al. 2007, ApJ, 671, 2129
Daassou, A., Benkhaldoun, Z., Ait Moulay Larbi, M., & Elazhari, Y. 2014, ArXiv e-prints
Desort, M., Lagrange, A.-M., Galland, F., Udry, S., & Mayor, M. 2007, A&A, 473, 983
Dumusque, X. 2014, ApJ, 796, 133
Dumusque, X., Boisse, I., & Santos, N. C. 2014, ApJ, 796, 132
Dumusque, X., Santos, N. C., Udry, S., Lovis, C., & Bonfils, X. 2011a, A&A, 527, A82
Dumusque, X., Udry, S., Lovis, C., Santos, N. C., & Monteiro, M. J. P. F. G. 2011b, A&A, 525, A140
Duncan, D. K., Frazer, J., Lanning, H. H., et al. 1984, PASP, 96, 707
Eker, Z. 1994, ApJ, 420, 373
Eker, Z., Brandt, P. N., Hanslmeier, A., Otruba, W., & Wehrli, C. 2003, A&A, 404, 1107
Eyer, L., Holl, B., Pourbaix, D., et al. 2013, Central European Astrophysical Bulletin, 37, 115
Fares, R., Donati, J.-F., Moutou, C., et al. 2010, MNRAS, 406, 409
Figueira, P., Santos, N. C., Pepe, F., Lovis, C., & Nardetto, N. 2013, A&A, 557, A93
Fontenla, J. M., Curdt, W., Haberreiter, M., Harder, J., & Tian, H. 2009, ApJ, 707, 482
Fontenla, J. M., Harder, J., Livingston, W., Snow, M., & Woods, T. 2011, Journal of Geophysical Research (Atmospheres), 116, 20108
Foukal, P. 1998, ApJ, 500, 958
Frazier, E. N. & Stenflo, J. O. 1978, A&A, 70, 789
Gondoin, P. 2008, A&A, 478, 883
Gray, D. F. 1992, The observation and analysis of stellar photospheres.
Hall, J. C., Lockwood, G. W., & Skiff, B. A. 2007, AJ, 133, 862
Haywood, R. D., Collier Cameron, A., Queloz, D., et al. 2014, MNRAS, 443, 2517
Henry, G. W., Eaton, J. A., Hamer, J., & Hall, D. S. 1995, ApJS, 97, 513
Henry, G. W. & Winn, J. N. 2008, AJ, 135, 68
Hussain, G. A. J. 2002, Astronomische Nachrichten, 323, 349
Husser, T.-O., Wende-von Berg, S., Dreizler, S., et al. 2013, A&A, 553, A6
Jackson, R. J. & Jeffries, R. D. 2013, MNRAS, 431, 1883
Jiang, J., Cameron, R. H., Schmitt, D., & Schüssler, M. 2011, A&A, 528, A82
Katsova, M. M., Livshits, M. A., & Belvedere, G. 2003, Sol. Phys., 216, 353
Kipping, D. M. 2012, MNRAS, 427, 2487
Kirkpatrick, S., Gelatt, C. D., & Vecchi, M. P. 1983, Science, 220, 671
Lagrange, A.-M., Desort, M., & Meunier, N. 2010, A&A, 512, A38

Lanza, A. F., Aigrain, S., Messina, S., et al. 2009, A&A, 506, 255
Lanza, A. F., Boisse, I., Bouchy, F., Bonomo, A. S., & Moutou, C. 2011a, A&A, 533, A44
Lanza, A. F., Bonomo, A. S., Moutou, C., et al. 2010, A&A, 520, A53
Lanza, A. F., Bonomo, A. S., Pagano, I., et al. 2011b, A&A, 525, A14
Lanza, A. F., Rodonò, M., Pagano, I., Barge, P., & Llebaria, A. 2003, A&A, 403, 1135
Léger, A., Rouan, D., Schneider, J., et al. 2009, A&A, 506, 287
Lindegren, L., Babusiaux, C., Bailer-Jones, C., et al. 2008, in IAU Symposium, Vol. 248, IAU Symposium, ed. W. J. Jin, I. Platais, & M. A. C. Perryman, 217–223
Livshits, M. A., Alekseev, I. Y., & Katsova, M. M. 2003, Astronomy Reports, 47, 562
Livshits, M. A. & Polonskii, V. V. 1968, Soviet Ast., 11, 965
Ludwig, H.-G., Caffau, E., Steffen, M., et al. 2009, Mem. Soc. Astron. Italiana, 80, 711
Ludwig, H.-G., Freytag, B., & Steffen, M. 1999, A&A, 346, 111
Marsden, S. C., Waite, I. A., Carter, B. D., & Donati, J.-F. 2005, MNRAS, 359, 711
Martinez Pillet, V., Moreno-Insertis, F., & Vazquez, M. 1993, A&A, 274, 521
McCullough, P. R., Crouzet, N., Deming, D., & Madhusudhan, N. 2014, ApJ, 791, 55
McQuillan, A., Aigrain, S., & Roberts, S. 2012, A&A, 539, A137
Melo, C., Santos, N. C., Pont, F., et al. 2006, A&A, 460, 251
Meunier, N., Desort, M., & Lagrange, A.-M. 2010a, A&A, 512, A39
Meunier, N., Lagrange, A.-M., & Desort, M. 2010b, A&A, 519, A66
Miller-Ricci, E., Rowe, J. F., Sasselov, D., et al. 2008, ApJ, 682, 593
Moulds, V. E., Watson, C. A., Bonfils, X., Littlefair, S. P., & Simpson, E. K. 2013, MNRAS, 430, 1709
Moutou, C., Donati, J.-F., Savalle, R., et al. 2007, A&A, 473, 651
Mullan, D. J. & MacDonald, J. 2001, ApJ, 559, 353
Nelson, B. & Davis, W. D. 1972, ApJ, 174, 617
Nourani, Y. & Andersen, B. 1998, J. Phys. A: Math. Gen, 31, 8373–8385
Olah, K. & Pettersen, B. R. 1991, A&A, 242, 443
O'Neal, D., Neff, J. E., Saar, S. H., & Cuntz, M. 2004, AJ, 128, 1802
Ortiz, A., Solanki, S. K., Domingo, V., Fligge, M., & Sanahuja, B. 2002, A&A, 388, 1036
Oshagh, M., Boisse, I., Boué, G., et al. 2013a, A&A, 549, A35
Oshagh, M., Santos, N. C., Boisse, I., et al. 2013b, A&A, 556, A19
Oshagh, M., Santos, N. C., Ehrenreich, D., et al. 2014, A&A, 568, A99
Padmakar & Pandey, S. K. 1999, A&AS, 138, 203
Penn, M. J. & MacDonald, R. K. D. 2007, ApJ, 662, L123
Pepe, F., Mayor, M., Galland, F., et al. 2002, A&A, 388, 632
Pepe, F., Mayor, M., Queloz, D., et al. 2004, A&A, 423, 385
Petrov, P. P., Shcherbakov, V. A., Berdyugina, S. V., et al. 1994, A&AS, 107, 9
Petrovay, K., Martínez Pillet, V., & van Driel-Gesztelyi, L. 1999, Sol. Phys., 188, 315
Petrovay, K. & van Driel-Gesztelyi, L. 1997, Sol. Phys., 176, 249
Pont, F., Gilliland, R. L., Moutou, C., et al. 2007, A&A, 476, 1347
Pont, F., Knutson, H., Gilliland, R. L., Moutou, C., & Charbonneau, D. 2008, MNRAS, 385, 109
Pont, F., Sing, D. K., Gibson, N. P., et al. 2013, MNRAS, 432, 2917
Popper, D. M. & Etzel, P. B. 1981, AJ, 86, 102
Pulkkinen, P. J., Brooke, J., Pelt, J., & Tuominen, I. 1999, A&A, 341, L43
Queloz, D., Henry, G. W., Sivan, J. P., et al. 2001, A&A, 379, 279
Robertson, P. & Mahadevan, S. 2014, ApJ, 793, L24
Rodonò, M., Messina, S., Lanza, A. F., Cutispoto, G., & Teriaca, L. 2000, A&A, 358, 624
Sanchis-Ojeda, R. & Winn, J. N. 2011, ApJ, 743, 61
Silva-Valio, A., Lanza, A. F., Alonso, R., & Barge, P. 2010, A&A, 510, A25
Sing, D. K., Pont, F., Aigrain, S., et al. 2011, MNRAS, 416, 1443
Snodgrass, H. B. & Ulrich, R. K. 1990, ApJ, 351, 309
Solanki, S. K. 1993, Space Sci. Rev., 63, 1
Solanki, S. K. & Unruh, Y. C. 2004, MNRAS, 348, 307
Southworth, J., Maxted, P. F. L., & Smalley, B. 2004, MNRAS, 351, 1277
Steinegger, M., Brandt, P. N., & Haupt, H. F. 1996, A&A, 310, 635
Stix, M. 2002, Astronomische Nachrichten, 323, 178
Strassmeier, K. G. 1992, in Astronomical Society of the Pacific Conference Series, Vol. 34, Robotic Telescopes in the 1990s, ed. A. V. Filippenko, 39–52
Strassmeier, K. G. 2009, A&A Rev., 17, 251
Strassmeier, K. G., Hall, D. S., & Henry, G. W. 1994a, A&A, 282, 535
Strassmeier, K. G. & Rice, J. B. 1998, in Astronomical Society of the Pacific Conference Series, Vol. 154, Cool Stars, Stellar Systems, and the Sun, ed. R. A. Donahue & J. A. Bookbinder, 2048
Strassmeier, K. G., Welty, A. D., & Rice, J. B. 1994b, A&A, 285, L17
Tessenyi, M., Ollivier, M., Tinetti, G., et al. 2012, ApJ, 746, 45
Triaud, A. H. M. J., Queloz, D., Bouchy, F., et al. 2009, A&A, 506, 377
Unruh, Y. C., Solanki, S. K., & Fligge, M. 1999, A&A, 345, 635
Vaughan, A. H., Preston, G. W., & Wilson, O. C. 1978, PASP, 90, 267
Vecchio, A., Laurenza, M., Meduri, D., Carbone, V., & Storini, M. 2012, ApJ, 749, 27
Vitense, E. 1953, ZAp, 32, 135
Wilson, O. C. 1978, ApJ, 226, 379
Winn, J. N., Holman, M. J., Henry, G. W., et al. 2007, AJ, 133, 1828
Winn, J. N., Johnson, J. A., Marcy, G. W., et al. 2006, ApJ, 653, L69
Wright, J. T., Marcy, G. W., Butler, R. P., & Vogt, S. S. 2004, ApJS, 152, 261

Table A.1. Parameters for the MC-SA algorithm as used in `StarSim`

Parameter	Value
T_0	1000
α	0.25
n_β	1000 – 10000
k	20

Appendix A: Simulated annealing procedure

We show here a simple outline of simulated annealing optimization method implemented in `StarSim`.

1. Draw a random configuration (a list of random spots).
   - Set initial inverse temperature $\beta = \beta_0$, where $T = 1/\beta$ is defined as the cooling temperature of the algorithm.
   - Let $k = 0$ (number of temperature steps).
   - Let $n_\beta = 0$ (number of steps for each temperature)
2. Make the current configuration ϕ_j evolve to a perturbed configuration ϕ_j^p by *slightly* modifying one randomly selected parameter of one of the spots.
3. If $\chi^2(\phi_j^p) < \chi^2(\phi_j)$ then
   accept ϕ_j^p
   else
   accept ϕ_j^p with probability $e^{-\beta\Delta\chi^2}$
   $n_\beta \leftarrow n_\beta + 1$. If $n_\beta \leq n_\beta^{MAX}$ go to 2.
4. Increase the inverse temperature $\beta \leftarrow \beta + \delta\beta$ according to a *cooling schedule*.
5. $k \leftarrow k + 1$. If $k < k_{max}$ go to 2, else go to 6.
6. End.

The great advantage of MC-SA is the ability of avoiding local extrema given an adequate *cooling schedule*, which is the way the temperature is decreased. Hence, a favourable configuration after a perturbation is always accepted while a disfavourable perturbation can be accepted or not according to an exponential probability, making it possible to *hillclimb* to finally reach the global optimum. There is no consistent rule to choose an optimal annealing schedule as it strongly depends on the specific problem to optimize. However, a fairly efficient scheme may be determined by trial and error (Kirkpatrick et al. 1983) to obtain a robust minimizer, and fast convergence was found for a Kirkpatrick cooling schedule,

$$\beta_k = \beta_0\, \alpha^{-k}, \tag{A.1}$$

in comparison to a linear scheme, both widely used since they were first introduced (Nourani & Andersen 1998). Several trials were carried out to adjust the parameters (T_0, α, n_β and k) until proper behavior was reached. Table A.1 summarizes the values of all MC-SA parameters as configured in `StarSim`.